Check for updates

AGU ADVANCING EARTH AND SPACE SCIENCE

Water Resources Research

RESEARCH ARTICLE
10.1029/2019WR025917

Transit Times and StorAge Selection Functions in Idealized Hillslopes With Steady Infiltration

Minseok Kim[1,2] and **Ciaran J. Harman**[1,3]

[1]Department of Environmental Health and Engineering, Johns Hopkins University, Baltimore, MD, USA, [2]Now at Biosphere 2, University of Arizona, Tucson, AZ, USA, [3]Department of Earth and Planetary Science, Johns Hopkins University, Baltimore, MD, USA

Key Points:

- StorAge Selection (SAS) functions are derived from steady state hydraulic groundwater theory for subsurface flow through idealized hillslopes
- Theory reproduces water age and transport in 2D models and experimental hillslopes, revealing hillslope structural controls on SAS functions
- Vertical transport in the unsaturated zone reduces the contribution of youngest storage to discharge, and Hillslope Number affects SAS shape

Supporting Information:

Supporting Information may be found in the online version of this article.

Correspondence to:

C. J. Harman,
charman1@jhu.edu

Citation:

Kim, M., & Harman, C. J. (2022). Transit times and StorAge Selection functions in idealized hillslopes with steady infiltration. *Water Resources Research*, *58*, e2019WR025917. https://doi.org/10.1029/2019WR025917

Received 2 JUL 2019
Accepted 31 JAN 2022

Author Contributions:

Conceptualization: Minseok Kim, Ciaran J. Harman
Data curation: Minseok Kim
Formal analysis: Minseok Kim
Funding acquisition: Ciaran J. Harman
Investigation: Minseok Kim
Methodology: Minseok Kim
Project Administration: Ciaran J. Harman
Resources: Minseok Kim
Software: Minseok Kim
Supervision: Ciaran J. Harman
Validation: Minseok Kim
Visualization: Minseok Kim
Writing – original draft: Minseok Kim

© 2022. The Authors.
This is an open access article under the terms of the Creative Commons Attribution License, which permits use, distribution and reproduction in any medium, provided the original work is properly cited.

Abstract Spatially integrated transport models have been applied widely to model hydrologic transport. However, we lack simple and process-based theoretical tools to predict the transport closures—transit time distributions (TTDs) and StorAge Selection (SAS) functions. This limits our ability to infer characteristics of hydrologic systems from tracer observations and to make first-order estimates of SAS functions in catchments where no tracer data is available. Here we present a theoretical framework linking TTDs and SAS functions to hydraulic groundwater theory at the hillslope scale. For hillslopes where the saturated hydraulic conductivity declines exponentially with depth, analytical solutions for the closures are derived that can be used as hypotheses to test against data. In the simplest form, the hillslope SAS function resembles a uniform or exponential distribution (corresponding to flow pathways in the saturated zone) offset from zero by the storage in the unsaturated zone that does not contribute to discharge. The framework is validated against nine idealized virtual hillslopes constructed using a 2-D Richards equation-based model, and against data from tracer experiments in two artificial hillslopes. Modeled internal age, life expectancy, and transit time structures reproduce theoretical predictions. The experimental data also support the theory, though further work is needed to account for the effects of time-variability. The shape and tailing of TTDs and their power spectra are discussed. The theoretical framework yields several dimensionless numbers that can be used to classify hillslope scale flow and transport dynamics and suggests distinct water age structures for high or low Hillslope number.

1. Introduction

StorAge Selection (SAS) functions and transit time distributions (TTDs) have been widely used to model catchment scale hydrologic transport (e.g., McGuire & McDonnell, 2006; van der Velde et al., 2012; Harman, 2015). Recently, SAS functions have been developed to capture controls on the time-variability of transit time distributions when flow rates and transport pathways through the system are variable in time. These functions capture the system-scale transport of conservative tracers in a form that is useful both for the interpretation of tracer data (e.g., Harman, 2015; Kim et al., 2016), and potentially for large-scale transport modeling.

In most applications of TTDs and the SAS functions, the functional forms of these functions have been chosen a priori, and the function's parameters were calibrated using observed tracer datasets (e.g., Benettin et al., 2017; McGuire & McDonnell, 2006). Those calibrated functions were mostly explained quantitatively but not mechanistically (e.g. Harman, 2015; van der Velde et al., 2014). While recent advances have been made in estimating TTDs without imposing functional forms *a priori* (Kim & Troch, 2020; Kirchner, 2019), these methods still do not provide mechanistic explanations. This, in part, results from the lack of parsimonious predictive tools relating TTD or SAS functions directly to hillslope and catchment scale properties. We have very limited and incomplete tools to explain the calibrated SAS functions, or even to make informed choices about appropriate functional forms to calibrate.

This challenge is similar to (and really an extension of) the challenge of finding simplified hydraulics and process-based theories (or models) that can predict the observed signatures of flow, such as the flow recession curves and the flow duration curves, at the hillslope or catchment scale. Some progress has been made in that area by developing simple theories based on idealized domains (e.g., the Boussinesq model (Boussinesq, 1877), the Hillslope-storage Boussinesq model (Troch et al., 2003), and TOPMODEL (Beven & Kirkby, 1979)), and using mechanistic understandings gathered from those models to frame hypotheses (Troch et al., 2013).

Writing – review & editing: Ciaran J. Harman

Such simple, idealized, hydraulics and process-based models have not been developed for hydrologic transport at the hillslope scale to the same extent. There are several studies that examined the theoretical linkage between the landscape's internal transport processes and TTDs. However, those models are not fully developed and are limited to models for 1-D domains (e.g., Cox & Miller, 1972), models for homogeneous 2-D semi-confined aquifers (Cornaton & Perrochet, 2006; Etcheverry, 2001; Fiori et al., 2009; Leray et al., 2012, 2016; Raats, 1978; Vogel, 1966), and models for homogeneous unconfined aquifers based on the Boussinesq model (Gelhar & Wilson, 1974; Haitjema, 1995). Theoretical TTDs based on such models do not reproduce spectral characteristics inferred from tracer datasets, for example, 1/f scaling (Godsey et al., 2010; Kirchner et al., 2000).

Kirchner et al. (2001) extended the 1-D model and showed that the hillslope scale dispersion must be on the order of the hillslope length in order to explain the 1/f scaling. However, this steady state, a one-dimensional theory is difficult to relate to actual processes since it is hard to quantify what contributes to the dispersion: it could be the local hydrodynamic dispersion (e.g., Taylor, 1953), the effect of self-organized macropore network (e.g., Sidle et al., 2001), or the difference between actual flow path length and those projected on the approximated one-dimensional flow paths. In other words, the actual flow pathways that the model simulates are somewhat obscure. The situation is similar in the recent studies of van Meerveld et al. (2019) and Rodriguez et al. (2020). In those studies, the flow path length and the water velocity are used to explain TTDs and the SAS functions, but it is not yet clear how to estimate the flow path length and the water velocity. The vertical dimension of the flow pathways and the water velocity variation along the flow pathway is not explicitly considered.

The two main purposes of this study are: first, to develop more complete but still parsimonious process and hydraulic theory-based models of flow and transport in idealized hillslope domains, and second, to use these to understand the relationship between the shapes of SAS functions and hillslope surface and subsurface structure. When estimated (or observed) SAS functions of a hydrologic system are available, the relationship can be used to develop a first-order hypothesis about the internal structures of the hydrologic system. We expect that such a first-order hypothesis can be validated (or invalidated) by other data, as the hypothesis is based on hydraulic theories that utilize soil hydraulic properties and geomorphologic structures. In addition, the parsimonious model of the TTDs or the SAS functions can be used as a first-order guess to describe system-scale transport dynamics when tracer data is not available but soil hydraulic properties and geomorphologic structures are known (or can be estimated). Furthermore, when developing the model, we seek dimensionless numbers that can be used to classify the hillslope scale water flow and transport dynamics.

Inspired by the work of Ameli et al. (2016), we will study the hillslope scale transport using the SAS function framework in a 2-D domain allowing for an exponential decline in permeability with depth. Though an idealization, this structure has been observed (e.g., Beven, 1982) and adopted in parsimonious models such as TOPMODEL (e.g., Beven & Kirkby, 1979). Ameli et al. (2016) found that TTD for 2-D numerical hillslope simulations had the properties necessary to reproduce the 1/f scaling of stream chemistry power spectra, indicating the importance of considering permeability structure of hillslopes.

In this work, analytically-derived SAS functions will be compared to numerically-simulated results from a Richards equation-based model (ParFlow, Maxwell et al. [2014]) and its particle tracking module (SLIM-FAST, Maxwell & Thomson [2006]). The corresponding generalized TTDs will also be presented to allow the results to be compared to previous studies of homogeneous aquifer.

As a first step toward a more general theory, we will consider hillslopes of constant width, planar surface slope, and saturated hydraulic conductivity that declines exponentially with depth. The analysis will focus on the effect of varying (a) the rate of exponential saturated hydraulic conductivity declines with depth and (b) topographic slope. For simplicity, and as we are currently at a very elementary level in this type of study, we restrict our analysis to steady state conditions. Also, the effect of local hydrodynamic dispersion is neglected.

We have chosen to limit our attention to steady state as the first step toward a more general understanding. We believe the steady state SAS functions are useful for providing first-order insights into unsteady transport dynamics. Previous work has shown that they can capture major features of experimental unsteady systems (Kim et al., 2016). This is an important difference from TTDs which fail to guarantee mass balance when they are directly applied to an unsteady system. Furthermore, we hypothesize that the SAS function is a better tool for linking lumped transport dynamics to internal structures as the SAS function is directly linked to actual turnover of water in storage (e.g., Rinaldo et al., 2015).

In Section 2 we will present the results of numerical modeling of nine virtual hillslopes. In Section 3 these will motivate and guide the analysis of controls of hillslope structure on TTDs and the SAS functions, and derivation of useful analytical and approximate expressions for TTDs and SAS functions that capture the effects of these controls. We will apply the analytical SAS function to two experimental hydrologic systems and discuss limitations in Section 4. We will conclude by suggesting ways these results might be used to guide further research.

2. Numerical Experiments

We performed 'virtual' (numerical) experiments in idealized hillslope domains using a Richards equation-based model and a particle tracking algorithm. In this section, we present brief description of the models and how we set up the hillslopes. We also present the numerical results of SAS functions and hillslope hydro-chronological structures.

2.1. Numerical Models

ParFlow (Maxwell et al., 2014) was used to simulate subsurface flow, and its particle tracking module, SLIM-FAST (Maxwell & Thomson, 2006), was used to simulate transport numerically. ParFlow simulates subsurface flow dynamics by solving Richards equation, which is given by:

$$\frac{\partial}{\partial t}\theta(\boldsymbol{x},t) = \nabla \cdot (k(\psi(\boldsymbol{x},t),\boldsymbol{x})\nabla(\psi(\boldsymbol{x},t)+z)) \tag{1}$$

where t is time, $\boldsymbol{x} = (x, y, z)$ is Cartesian spatial coordinate, θ is water content, k is hydraulic conductivity, ψ is suction head (defined as negative when pressure is below atmospheric).

The particle tracking module SLIM-FAST (Maxwell & Thomson, 2006) solves particle trajectories based on the estimated velocity field $\boldsymbol{V}(\boldsymbol{x}, t) = -k(\theta(x, t), \boldsymbol{x})\nabla(\psi(\boldsymbol{x}, t) + z)/\theta(\boldsymbol{x}, t)$ as:

$$\frac{d}{dt}\boldsymbol{x}_n(t) = \boldsymbol{V}(\boldsymbol{x}_n, t) \tag{2}$$

where n is an index that labels each particle, and $\boldsymbol{x}_n$ is the location of the particle n at time t.

ParFlow employs a cell-centered finite difference scheme to solve Richards equation (e.g., Jones & Woodward, 2001; Kollet & Maxwell, 2006), meaning that $\boldsymbol{V}$ is estimated at the center of grid elements. SLIM-FAST linearly interpolates the velocity at points of interest using the cell-centered velocity field $\boldsymbol{V}$, following the method of Pollock (1988).

2.2. Description of Virtual Hillslopes

We considered nine virtual hillslopes that differed in their topographic slope and the length scale of the exponential saturated hydraulic conductivity decline with depth. The topographic surface $H(x)$ of the hillslopes was assumed to be planar, and described by $H(x) = H_L + (L - x)\tan\beta$, where x is horizontal location, L is the hillslope length, H_L is the height of the outflow boundary at $x = L$, and β is the slope of the surface. H_L was set to 3 m, and L was set to 80 m. Three values were applied for $\tan\beta$: $\tan\beta \in \{0.05, 0.15, 0.30\}$.

The saturated hydraulic conductivity field $k_s(x, z)$ was constructed by assuming that the surface hydraulic conductivity is constant value k_0 at the topographic surface, and then declines with depth as:

$$k_s(x,z) = k_0 e^{-(H(x)-z)/P} \quad (\text{when } 0 \le z \le H(x)) \tag{3}$$

where P is the decline length scale (e-folding depth). The surface hydraulic conductivity k_0 was chosen differently for each case so that the transmissivity (vertically integrated hydraulic conductivity $= \int_0^L \int_0^H k_s(x,z)dzdx/L$) is the same value (12.5 m^2/day) for the all cases. Three decline length scales were considered: $P \in \{0.5$ m, 2.0 m, $\infty\}$. When $P \to \infty$ the conductivity is homogeneous. The combination of three decline length scales and slopes generates the nine hillslopes shown in Figure 1.

The van Genuchten model was used to describe the soil-water retention characteristic, which can be written as (van Genuchten, 1980): $\theta(\psi) = \theta_r + (\theta_s - \theta_r)\left(1 + |\psi/\psi_A|^n\right)^m$ where θ is water content, θ_r is residual water

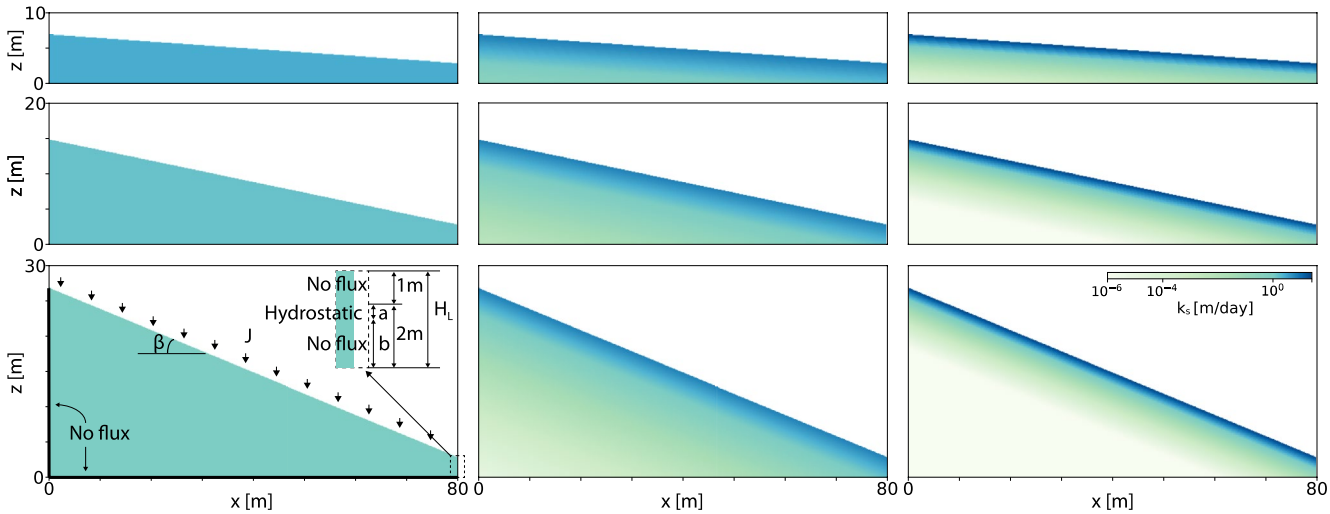

Figure 1. Structure of the nine virtual hillslopes used to compare numerical solutions to the analytical results. Three slopes were considered ($\tan\beta \in \{0.05, 0.15, 0.30\}$), and three rates of decline of hydraulic conductivity (e-folding depths $P \in \{0.5\,\text{m}, 0.2\,\text{m}, \infty\}$, where ∞ represents the homogeneous case). Color represents the hydraulic conductivity.

content, θ_s is saturated water content, ψ is suction pressure head ($\psi < 0$), ψ_A is a parameter sometimes referred to as the air-entry pressure, n is the parameter related to the pore-size distribution, and $m = 1 - 1/n$. The van Genuchten-Mualem relationship (van Genuchten, 1980) was used to describe the relative hydraulic conductivity: $k_r(\psi) = (1 + |\psi/\psi_A|^n)^{-m/2}\left(|\psi/\psi_A|^{-1+n}(1 + |\psi/\psi_A|^n)^{-m} - 1\right)^2$. Parameters used in the numerical simulations were: $\theta_s = 0.4$, $\theta_r = 0.01$, $\psi_A = 0.2$ m, and $n = 2$, which are typical values for loamy sand (Harman & Kim, 2019). The values for ψ_A and n are similar (though not identical) to those of the soil used in the Landscape Evolution Observatory (LEO), Biosphere 2, The University of Ariozna, Tucson, AZ, USA (e.g., Pangle et al., 2015).

Boundary conditions for flow and transport models are required for each side of the hillslopes: the most upslope ($x = 0$), the horizontal impermeable layer ($z = 0$), the soil surface ($z = H(x)$ for $x \in [0, L]$), and the outlet ($x = L$). A no-flux boundary condition was imposed at the upslope and horizontal boundaries: $\frac{dh}{d\xi} = 0$ where ξ is the co-ordinate orthogonal to the boundary. At the soil surface, a constant flux boundary condition was set to simulate steady state infiltration of 5 mm/day, which could represent the mean recharge rate during a wet season in a humid climate, or during snowmelt. For the downslope boundary condition, the water table was assumed to be determined by the water level in an adjacent stream zone, and fixed at $z = 2$ m. A no-flux condition was set for the unsaturated zone above the water table $z \in (2\,\text{m}, H_L]$. Below the water table, the boundary condition is no-flux for $z \in [0, 1.9\,\text{m})$, and it is hydrostatic (of 2 m) along $z \in [1.9\,\text{m}, 2\,\text{m}]$. (This boundary condition is similar to that used in Ameli et al. [2016]).

The grid spacing was set to 0.05 m, and the computation time step was set to grow from 0.00001s to 1 day with the rate of 1.5. The model was run to steady state and the final flow field was used to drive particle tracking in SLIM-FAST. 10,000 particles were introduced 0.01 m below the surface, evenly across the hillslopes. These were considered to have exited the domain when they crossed the seepage face at the right hand boundary, and the model was run for 5000 days after introducing the particles.

2.3. Hydro-Chronological Structure of Storage and Discharge

2.3.1. StorAge Selection Function

The transport behavior of the hillslopes was examined by calculating the StorAge Selection (SAS) function, Ω_Q. As this approach is still relatively new, we will introduce the function briefly. For more details see for example, Harman (2015). In the SAS function framework, the age-ranked storage $S_T = S_T(T, t)$ is an un-normalized form of the cumulative residence time distribution (volume of water younger than an age T at time t). The SAS function

is equal to the cumulative (backward) transit time distribution $\overleftarrow{P_Q}(T,t)$ under a change of variables $T \rightarrow S_T$, that is, $\Omega_Q(S_T(T),t) = \overleftarrow{P_Q}(T,t)$.

The governing equation of the SAS function framework, which solves time-variable transport dynamics, is (Harman, 2015):

$$\frac{\partial}{\partial t}S_T(T,t) = J(t) - Q(t)\overleftarrow{P_Q}(T,t) - \frac{\partial}{\partial T}S_T(T,t) \tag{4}$$

which can be solved (with the boundary condition $S_T(0), t = 0$) to determine how S_T evolves in time. $\overleftarrow{P_Q}(T,t)$ can be obtained from $\overleftarrow{P_Q}(T,t) = \Omega_Q\left(S_T(T,t),t\right)$ at each moment in time.

Under steady state, the governing equation can be written as:

$$\frac{d}{dT}S_T(T) = Q\left(1 - P_Q(T)\right) = Q\left(1 - \Omega_Q\left(S_T(T)\right)\right) \tag{5}$$

where $\Omega_Q(S_T)$ is the SAS function and $P_Q(T)$ is the transit time distribution under steady state. The forward and backward TTDs are equivalent in this case, and so the arrow will be dropped from the notation. This equation can be used to relate the SAS function to a steady state equivalent TTD.

Particle tracking allows us to estimate the transit time distribution $P_Q(T)$ by counting the fraction of injected particles that exit the hillslope prior to time T. This was done for each time step ΔT, which was set to 1 day for all simulations. Using the transit time distribution, the age-ranked storage $S_T(T)$ was estimated through Equation (5). The SAS function Ω_Q can then be obtained by plotting $P_Q(T)$ against corresponding values of $S_T(T)$ with the same T, that is: $\Omega_Q(S_T(T)) = P_Q(T)$.

The dark grey lines in Figure 2 illustrate the resulting StorAge Selection (SAS) functions for all the considered cases. The relationship between hillslope structures and these SAS functions will be considered closely in Section 2.4 and Section 3, but here we can describe some general trends. The SAS functions were mostly linear for the homogeneous cases and showed more convexity as P decreases; that is, as saturated hydraulic conductivity declines more sharply, the SAS function skewed toward to the younger water in the storage. This means that the hillslopes with sharper hydraulic conductivity declines with depth transmit a larger young fraction of water. The effect of surface topographic gradient on the SAS function is more subtle though.

2.3.2. Internal Age, Life Expectancy, and Transit Time Structures

Particle tracking also allowed us to explore internal water age structure. Internal water age structure $A(\boldsymbol{x})$ is an important control on geochemical transformations taking place in a system, as it represents the exposure time of water to the system's condition (e.g., Gomez & Wilson, 2013; Maher, 2011). In addition to the age structure, spatial life expectancy and transit time structure also can be examined through particle tracking. By definition, the life expectancy $LE(\boldsymbol{x})$ is the time that will be required for a particle starting at location $\boldsymbol{x}$ to exit the system. The ultimate transit time T of any parcel is the sum of the two: $T(\boldsymbol{x}) = A(\boldsymbol{x}) + LE(\boldsymbol{x})$ (e.g., Benettin et al., 2013; Cornaton & Perrochet, 2006). While the transit time T has usually been examined for water exiting a system, it is also possible to construct the internal (spatial) transit time distribution, which will be a constant along the trajectory of a given particle.

Figure 3 illustrates the internal water age, life expectancy, and transit time structures for the low and high slope cases at the end of the virtual experimental period (5000 days after introducing particles). In many cases, the water age shows limited variability downslope (either parallel to the base impermeable layer in the homogeneous case, or to the soil surface in the others). Younger water layers 'stack' above the older water layers. The structure is slightly different for the steep homogeneous case ($P \rightarrow \infty, \tan\beta = 0.30$), where age contours are parallel to the surface in the unsaturated zone, and appear to refract at the saturated interface to become more parallel to the base. Contours of life expectancy in the saturated zones are mostly orthogonal to the impermeable layer in the homogeneous case ($P \rightarrow \infty$), meaning that water particles along a vertical line take a similar amount of time to get to the outlet. In the unsaturated zone, the contour lines are tilted toward the outlet, as water particles located at upper locations take more time to exit the hillslope. For sharper declines in hydraulic conductivity, the contours of life expectancy in the saturated zone tilt away from the outlet, reflecting the fact that water higher in the profile is on a faster track to the outlet. The hydraulic conductivity is lower, deeper in the profile, and so, water

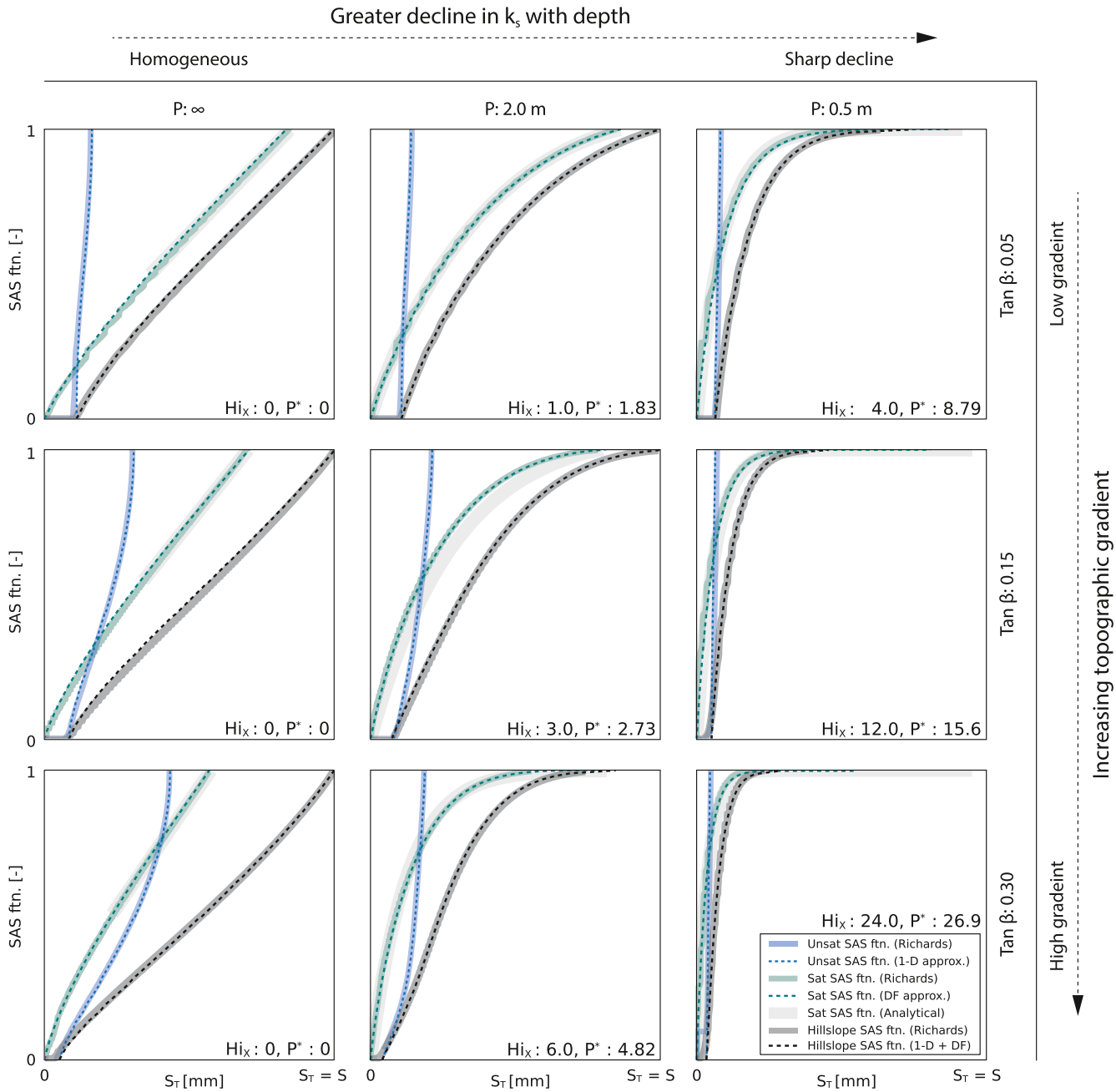

Figure 2. The estimated StorAge Selection (SAS) functions in the nine idealized hillslopes. (Black and dark gray lines) the SAS functions for the hillslopes as a whole. (Blue lines) the SAS functions for the unsaturated zone. (Green and light gray lines) the SAS functions for the saturated zone. The bold lines of the colors (except light gray) are the SAS function estimated using the Richards equation based model and the particle tracking module. The dotted lines are the functions estimated using a simplifying assumption, the 1-D approximation or the Dupuit-Forchheimer assumption. The bold light gray lines are the analytical solutions for the saturated zone SAS function using Equation (26). In each plot, S_T is scaled accordingly to fit the hillslope scale SAS functions to the size of the plots.

particles located lower will take more time to get to the outlet. The transit time structures are also illustrated in Figure 3, where the contour lines correspond to the flow pathways because water particles along a flow trajectory have identical transit time. The pathways show that the water particles move mostly vertically in the unsaturated zone, and then turn toward the outlet once they pass through the water table.

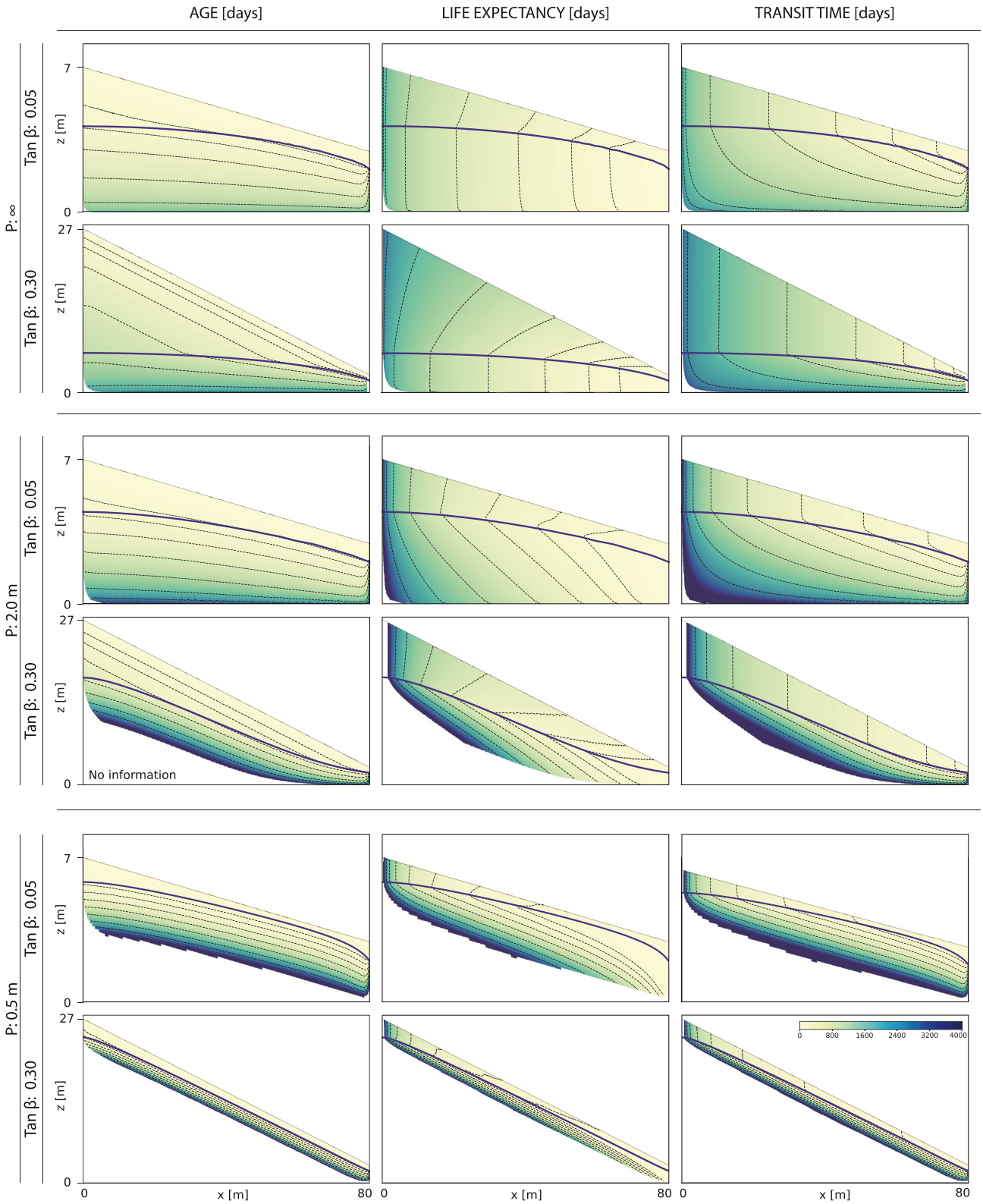

Figure 3. (left) age, (middle) life expectancy, and (right) transit time structures for the six selected cases. The dotted contour lines are drowned at 50, 100, 200, 400, 800, 1500, and 2500 days, and the thick dark lines indicate the water table. The white area inside the hillslopes is where no information is available because either age or life expectancy is higher than 5000 days, which is the virtual experimental period.

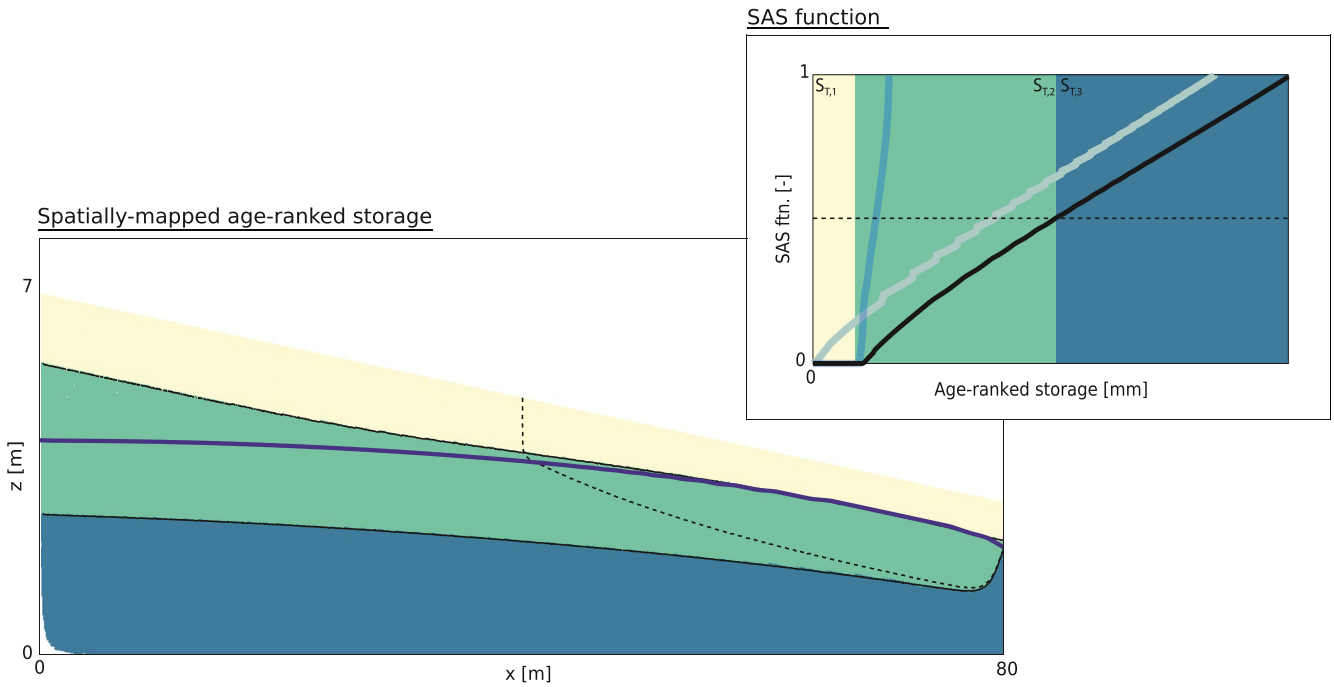

Figure 4. (left) Low slope, homogeneous hillslope ($\tan\beta = 0.05$ and $P \rightarrow \infty$) decomposed into three ranges of age-ranked storage. The thick blue line illustrates the water table. (right) The estimated hillslope StorAge Selection (SAS) function for this case (black line). The blue and green lines show the SAS function for the unsaturated zone and the saturated zone, respectively. The dotted line in the right figure illustrates at what fraction of discharge the hillslope SAS function becomes linear. In the left figure, the dotted line illustrates the flow pathway that separates the linear and the non-linear part of the SAS function; for example, water infiltrates through the left part of the line resulting in the linear hillslope SAS function.

2.4. Decomposition of Saturated and Unsaturated Age and SAS Function Structure

The contrasting behavior of the saturated and unsaturated zone seen above suggests that we should look at their individual contributions to the overall SAS function. Figure 4 shows the low-gradient, homogeneous slope ($P \rightarrow \infty$ and $\tan\beta = 0.05$) and its corresponding SAS function (black line in the inset figure). The SAS function shows three distinct types of behavior across the range of age-ranked storage. For values of S_T below a threshold, the SAS function is zero (yellow region), indicating that no water from these age-ranks in storage is discharged. In the middle range of S_T (green region) the SAS function shows convexity, which indicates that younger water (just older than the threshold) is preferentially discharged relative to older water. The SAS function gradually becomes linear in the last region, meaning that discharged water is drawn from all age-ranked storage uniformly (without preference for younger or older). The division between the second and third regions was chosen to correspond to the median transit time (so water in storage with higher S_T is already older than half the water is when it exits).

We can start to understand the origins of these distinct regions and their relationship to structure by mapping them back onto the spatial distribution of age in the hillslope, as shown in the left part of Figure 4. The threshold value of S_T separating the first and second parts of the SAS function corresponds with the age rank of the youngest water entering the saturated zone close to the hillslope toe. The threshold value of S_T does not precisely separate the saturated and unsaturated zone throughout the hillslope, as there are upslope unsaturated areas with larger S_T (green region). The third range of S_T (blue) represents water that entered the saturated zone in the upper part of the hillslope, where the water table gradient was relatively low. This is illustrated by the trajectory (black dotted line) of a particle injected half way up the hillslope, which eventually converges to the boundary between the second and third region as it moves down to the outlet.

Further insight can be obtained by separating the entire hillslope control volume into two distinct control volumes for the unsaturated zone (with infiltration as the inflow and recharge to the saturated zone as the outflow) and the saturated zone (with recharge as the inflow and discharge from the hillslope toe as the outflow), and considering their separate SAS functions (see the blue and green lines in Figures 2 and 4). In most cases, the unsaturated zone SAS function is a relatively narrow S-curve offset from zero, which suggests that water reaching the saturated

zone has a narrow range of ages, but none is younger than some threshold. The saturated zone SAS function shows a similar pattern to the overall hillslope SAS function, but without the offset from zero – for the homogeneous case it displays some convexity for younger age-ranked storage, but is linear for older one, while for the exponentially declining k_s it is generally convex.

3. Analysis and Analytical Solutions for Hillslope Flow and Transport

3.1. Overview

The results above suggest that the structure of the SAS function can potentially be explained by the internal structure of storage and flow paths. The unsaturated zone is largely acting like plug (or 'piston') flow, which we might expect given the primarily-vertical flow paths and (assumed) absence of dispersion. The approximately uniform SAS function of the homogeneous k_s saturated zone is also close to the behavior that would be expected from established theory. Gelhar and Wilson (1974) and others have shown that idealized aquifers with nearly-horizontal upper recharge boundaries have exponential TTD at a steady state, which corresponds with uniform SAS functions.

But there are aspects of the modeled behavior that are less easily understood. Why is the SAS function slightly convex for the middle range of age-ranked storage in the homogeneous case (indicating preferential release of young water from that storage)? For the non-homogeneous cases, is there a predictable relationship between the shape of the SAS function and the rate of decline in k_s with depth? And how do the SAS functions for the unsaturated and saturated zones 'add up' to produce the hillslope scale behavior?

Here we will examine the observed behavior in the light of simplified expressions of the flow hydraulics. Our aim is to develop functional forms for the SAS functions that are directly tied to the physical hillslope structure. There is a rich literature in hydraulic groundwater theory that we will draw on to accomplish this. Some key previous results are summarized below.

As the results above show, the spatial organization of saturated and unsaturated zones in the hillslope are extremely important and must be predicted first in order to determine the hillslope SAS function. The Boussinesq equation provides a prediction of the location of the water table for a homogeneous conductivity aquifer (e.g., Brutsaert, 1994). This model estimates the water table height h above a horizontal impermeable layer under steady state as (Boussinesq, 1877):

$$h(x) = \sqrt{h_L^2 + \frac{J(L^2 - x^2)}{k_s}} \tag{6}$$

where J is influx (or recharge) rate at the water table, L is length of hillslope, and x is distance from the most upslope, and h_L is the Dirichlet boundary condition for h at $x = L$. (See the bottom left panel of Figure 1).

When the impermeable layer is sloping, the total hydraulic gradient can be decomposed into contributions from the gradient of that underlying layer, and from the varying thickness of the aquifer itself. In the limit of a thin layer of saturation overlying a steeply sloping base the effect of the latter is minimal, and there arises a quite different spatial organization of lateral flux rate, saturated thickness, and flow paths from that which applies in the case of Equation (6) (Harman & Sivapalan, 2009; Harman & Kim, 2019). The relative contributions can be quantified by a dimensionless number suggested by Brutsaert (1994), known as the Hillslope number: $\mathrm{Hi} = L\tan\eta/(2\overline{H})$, where $\tan\eta$ is the slope of the base and $\bar{H}$ is an effective thickness of the saturated aquifer. This dimensionless number arises naturally in linearized solutions to the Boussinesq equation (Brutsaert, 1994), and controls the nature of the transient response in numerical solutions (Harman & Sivapalan, 2009). Although we will only consider cases with $\mathrm{Hi} = 0$, we will propose in the next section a modified form of this appropriate for the case where an exponentially declining k_s makes the effective thickness and driving slope different from the saturated thickness and impermeable base slope.

Several forms of TTD have been suggested based on simplified process-based models under certain assumptions. Vogel (1966) derived the (cumulative) TTD for a homogeneous semi-confined aquifer as:

$$P_Q(T) = 1 - e^{-\frac{T}{T_m}} \tag{7}$$

where $T_m = H_e\theta_s / J$ is the mean transit time, H_e is the thickness of the aquifer, and J is the influx. Gelhar and Wilson (1974) showed that this expression is valid for the Boussinesq type aquifer as long as the water table height difference between the most upslope and the most downslope is small enough compared to the most downslope water table height. Haitjema (1995) derived an implicit form of TTD for the Boussinesq aquifer and showed that the model Equation (7) works effectively when the averaged water table height is used for H_e, regardless of the relatively large water table difference.

Bredenkamp and Vogel (1970) further showed that the TTD is also exponential for semi-confined aquifers if the saturated hydraulic conductivity and the porosity decline with depth at the same rate. However, to capture the behavior in a truly unconfined hillslope aquifer we need a different approach.

3.2. Hybrid Boussinesq-TOPMODEL for Water Table Prediction

TOPMODEL, in its original form (Beven & Kirkby, 1979), was based on the assumption of an exponentially declining k_s, and we will adapt this approach, but augment it with an alternative approach to estimating the gradient driving flow. If we assume that under quasi-steady state the upslope recharge Jx (where x is the distance from the watershed divide, and thus also the accumulated upslope area per unit contour width in a straight hillslope) is balanced by the lateral flow according to Darcy's Law, we can write: $Jx = -K_H(x)dh/dx$ where $K_H(x)$ is transmissivity, and dh/dx is the hydraulic gradient. If the depth to the water table is D ($= H - h$ where H is the soil surface elevation) and k_s is declining exponentially to the impermeable boundary the transmissivity is given by $K_H = k_0 P(e^{-D(x)/P} - e^{-H(x)/P})$. Rearranging, this gives the depth to the water table as:

$$D(x) = P \ln\left(e^{-\frac{H(x)}{P}} + \frac{Jx}{k_0 P \tan\beta}\right) \tag{8}$$

TOPMODEL also adopted the 'kinematic wave' assumption—that is, that the hydraulic gradient in Darcy's law can be reasonably approximated by the surface topographic gradient. This contrasts with the Boussinesq equation, which is based on the Dupuit-Forchheimer assumption that the hydraulic gradient may be distinct from the surface topographic gradient, but that it is well approximated in each vertical section of the aquifer by the water table gradient.

Here we will use a hybrid of these models by adopting an exponential decline in k_s with depth, but relaxing the kinematic wave assumption in TOPMODEL, and replacing it with the Dupuit-Forchheimer assumption. In this case we can write the continuity equation to estimate the water table height h above the impermeable layer as:

$$\phi\frac{\partial h(x,t)}{\partial t} = k_0\frac{\partial}{\partial x}\left(\frac{\partial h(x,t)}{\partial x}\int_0^{h(x,t)} e^{-(H(x)-z)/P}dz\right) + J(t) \tag{9}$$

where ϕ is drainable porosity. At steady state the left hand side of Equation (9) is zero.

We will adopt boundary conditions commonly used to represent hillslope domains: a no-flux boundary at the upslope end at $x = 0$, so $q_x(x) = -k_0\frac{\partial h(x,t)}{\partial x} \times \int_0^{h(x,t)} e^{-(H(x)-z)/P}dz = 0$ at $x = 0$; and a fixed head or fixed gradient at the downslope end, representing the connection between the hillslope and riparian zones, so $h = h_L$ (fixed head) or $\frac{\partial h}{\partial x} = h'_L$ (fixed gradient) at $x = L$. (Note that the above continuity equation is similar to that of Rupp and Selker (2005) for the power-law decay of saturated hydraulic conductivity with depth).

This equation reduces to both the TOPMODEL governing equation and the Boussinesq model as special cases. The governing equation of TOPMODEL can be obtained when the hydraulic head gradient term $\frac{\partial h}{\partial x}$ is set by the surface slope $-\tan\beta$. The no-flux boundary condition at the most upslope is $h(0, t) = 0$ for this case (as $\tan\beta \neq 0$), since that is the only way to set zero flux with the kinematic wave assumption. This boundary condition is implicitly used in TOPMODEL to keep water mass balance. The depth to the water table, in this case, can be estimated using: Equation (8). The Boussinesq model, Equation (6), can be recovered when $P \to \infty$.

Note that when P is small relative to the relief of the hillslope $L\tan\beta$, the deeper part of the aquifer is effectively impermeable, and the water table becomes shallower to accommodate the required flow. Consequently, the overall hydraulic gradient is more strongly related to the imposed slope of the ground surface than to the varying thickness of the saturated aquifer. This is not captured by the Hillslope number Hi defined above. We can define

an alternative Hillslope number that applies in this case by examining linearized solutions to Equation (9) in a similar manner to previous studies in homogeneous Boussinesq aquifers (e.g., Berne et al., 2005; Brutsaert, 1994) (see Appendix A for more details). This suggests an exponential Hillslope number can be usefully defined as:

$$\mathrm{Hi}_X = \frac{L\tan\beta}{2P} \tag{10}$$

For the Dirichlet (fixed depth) boundary condition $D(L) = D_L = H_L - h_L$ and the linear soil surface $H(x) = H_L + (L - x)\tan\beta$ used in the simulations described in the previous section, the above equation yields the following analytical solution under steady state (expressed in dimensionless form using the relief $H_t = H(0) - H_L = L\tan\beta$ to non-dimensionalize vertical length scales, and L for horizontal length scales):

$$\begin{aligned}\hat{D}(\hat{x}) = \quad & \hat{H}(\hat{x}) - \hat{R}_L + Me^{2\mathrm{Hi}_X\hat{H}(\hat{x})}\left(\frac{1}{2\mathrm{Hi}_X} + \hat{x}\right) \\ & + \frac{1}{2\mathrm{Hi}_X} W_{-1}\left(-exp\left(2\mathrm{Hi}_X\left(\hat{R}_L - Me^{2\mathrm{Hi}_X\hat{H}(\hat{x})}\left(\frac{1}{2\mathrm{Hi}_X} + \hat{x}\right)\right)\right)\right)\end{aligned} \tag{11}$$

where $\hat{D} = \frac{D}{H_t}$, $\hat{x} = \frac{x}{L}$, $M = \frac{J}{k_0(\tan\beta)^2}$, $\hat{H}(\hat{x}) = \hat{H}_L + (1 - \hat{x})$, and $W_{-1}(\cdot)$ is lower branch of the Lambert-W function (which always yields values less than -1 [Corless et al., 1996]). $\hat{R}_L$ depends on the boundary condition:

$$\hat{R}_L = \hat{H}_L - \hat{D}_L - \frac{e^{2\mathrm{Hi}_X(\hat{H}_L - \hat{D}_L)}}{2\mathrm{Hi}_X} + Me^{2\mathrm{Hi}_X\hat{H}_L}\left(\frac{1}{2\mathrm{Hi}_X} + 1\right) \tag{12}$$

where $\hat{H}_L = \frac{H_L}{H_t}$, $\hat{D}_L = \frac{D_L}{H_t}$.

An analytical solution for the Neumann boundary condition (fixed gradient) and its comparison to the TOPMODEL solution are given in Appendix A. Equation 11 is presented in a dimensionless form to clarify the essential controls. (Note that the applied non-dimensionalization scheme is similar to that of Koussis [1992] and Harman & Sivapalan [2009]). The equation is a function of four dimensionless parameters: $\hat{H}_L$ and $\hat{D}_L$ which are related to the downslope boundary conditions, the dimensionless recharge rate M, and the exponential Hillslope number Hi_X. When $\mathrm{Hi}_X \to 0$, the solution approaches that predicted by the Boussinesq model, while the results approach those that might be obtained by TOPMODEL when Hi_X is large enough. (See Appendix A for more details.).

Figure 5 illustrates the water table height (or depth to water table) estimated by the numerical model and the solution presented above. As we can see, the solution matches the Richards equation-based simulation results. This suggests that the Dupuit-Forchheimer assumption is valid for the considered cases even with the exponential decline in hydraulic conductivity with depth.

3.3. Unsaturated Zone Transport

Having developed some useful tools to determine the separation between the saturated and unsaturated zones, we can now consider transport through each. For the unsaturated zone, the numerical solutions suggest that we may (in this idealized, steady state case) approximate the transport as a collection of piston flow systems. A piston flow system has a (cumulative) transit time distribution given by a step-function located at the single age—All discharge from the system acquires this age the moment it leaves. The final age $T_u(x)$ of a parcel of water moving vertically through the unsaturated zone at downslope location x can be calculated as:

$$T_u(x) = \int_0^{D(x)} \frac{1}{v\left(x, h(x) - z'\right)} dz' = \frac{1}{J}\int_0^{D(x)} \theta\left(x, h(x) - z'\right) dz' = \frac{S_u(x)}{J} \tag{13}$$

where v is the velocity field, J is the influx rate, θ is water content, and $S_u(x)$ is the unsaturated zone storage at x. That is, $T_u(x)$ is simply the time required to displace the resident water in the unsaturated zone.

Since these strips are operating in parallel, the (cumulative) transit time distribution $P_{Q,u}$ is a linearly-scaled (cumulative) histogram of the unsaturated zone storage $S_u(x)$ $\forall x \in [0, L]$, which can be formulated as:

$$P_{Q,u}(T) = \frac{1}{L}\int_0^L \mathbf{H}\left(T - T_u(x)\right) dx = \frac{1}{L}\int_0^L \mathbf{H}\left(JT - S_u(x)\right) dx \tag{14}$$

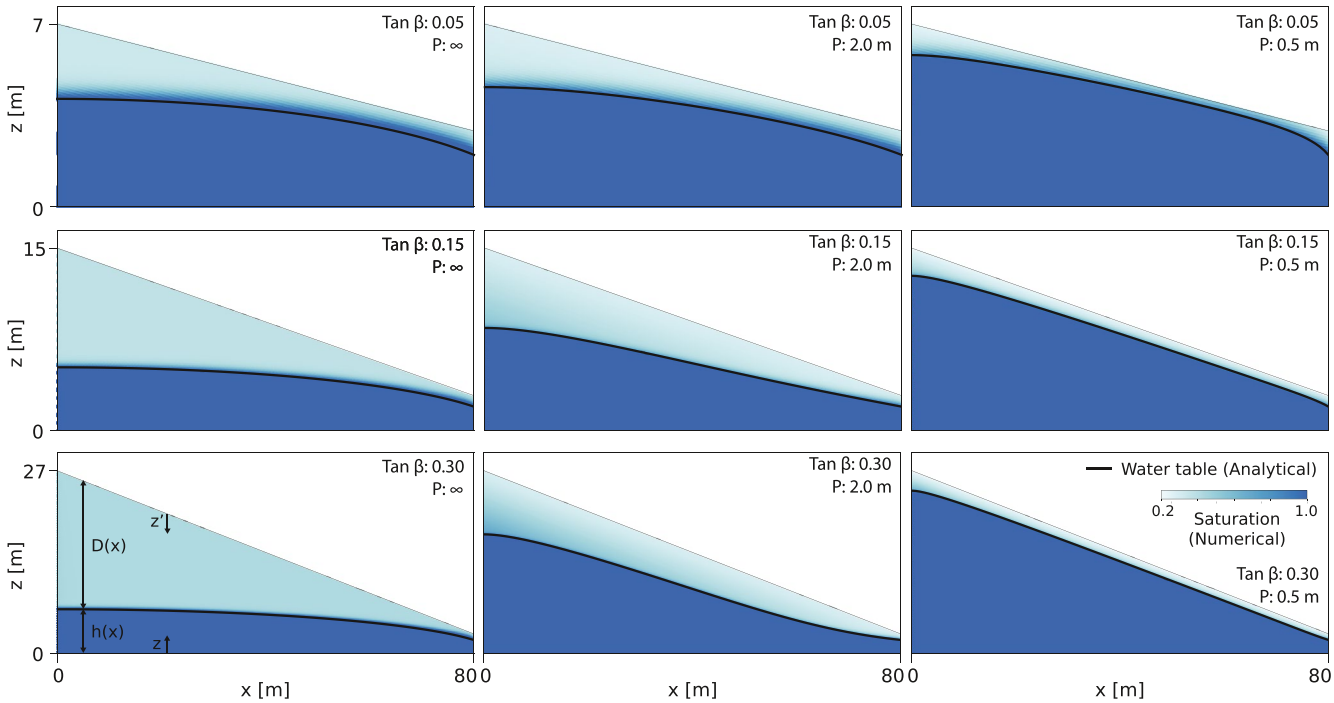

Figure 5. Saturation structure estimated using ParFlow (color represents saturation) and the water table (dark line) estimated using the hybrid Boussinesq-TOPMODEL Equation (11).

where $\mathbf{H}(\cdot)$ is the Heaviside (or unit) step function (Abramowitz & Stegun, 1974).

The unsaturated zone age-ranked storage $S_{T,u}$ can be estimated using Equation (5). This turns out to be:

$$S_{T,u}(T) = JT - \frac{1}{L}\int_0^L (JT - S_u(x))\,\mathrm{H}\,(JT - S_u(x))\,dx \tag{15}$$

$$= \frac{1}{L}\int_0^L \min\,(JT, S_u(x))\,dx \tag{16}$$

The SAS function can be obtained by eliminating T between the two equations above and setting $P_{Q,u}\,(T) = \Omega_{Q,u}\,(S_{T,u}\,(T))$. This can be expressed in compact form by inverting (15) for JT by defining $f^{-1}(S_{T,u}) = JT$:

$$\Omega_{Q,u}\,(S_{T,u}) = \frac{1}{L}\int_0^L \mathbf{H}\left(f^{-1}\,(S_{T,u}) - S_u(x)\right)dx \tag{17}$$

Unlike the TTD and age-ranked storage, the SAS function is not a direct function of J (though the unsaturated zone storage $S_u\,(x)$ does depend on J). This characteristic is related to the "internal" and "external" variabilities suggested in Kim et al. (2016). The shape of the SAS function depends on the current internal organization of storage (which is conditioned by the past history of inputs), and not directly on the external variability of the time history of recharge (Kim et al., 2016; Wilusz et al., 2017). In the current discussion in steady state, this means that the unsaturated zone SAS function is only related to the unsaturated zone thickness and unsaturated zone saturation structure, and it does not directly relate to the infiltration or recharge rate. Thus, the problem of estimating the SAS function (or the TTD) reduces to the one-dimensional problem of estimating the unsaturated zone storage $S_u\,(x)$ for all $x \in [0, L]$.

This can be further broken down into finding the depth to the water table $D(x)$ and the vertically-averaged water content $\bar{\theta}(x)$. If we can approximate the relationship between $D(x)$ and $\bar{\theta}(x)$, a simple form of transit time distribution and the SAS function is maybe obtainable. For example, if $S_u(x)$ varies linearly along the hillslope between a minimum of $\bar{\theta} D_{min}$ and a maximum of $\bar{\theta} D_{max}$ (i.e., $S_u(x) = \bar{\theta} D_{min} + \bar{\theta}\,(D_{max} - D_{min})\,x$), the TTD, the age ranked storage and the SAS function are given by the equations above as:

$$P_{Q,u}(T) = \left(1 - \frac{\bar{\theta}D_{\max} - JT}{\bar{\theta}D_{\max} - \bar{\theta}D_{\min}}\right) \mathrm{H}\left(JT - \bar{\theta}D_{min}\right) \quad \text{for } 0 \le T \le \bar{\theta}D_{\max}/J \tag{18}$$

$$S_{T,u}(T) = JT - \left(JT - \frac{\bar{\theta}D_{\max} + \bar{\theta}D_{\min}}{2} + \frac{\left(\bar{\theta}D_{\max} - JT\right)^2}{2\left(\bar{\theta}D_{\max} - \bar{\theta}D_{\min}\right)}\right) \mathrm{H}\left(JT - \bar{\theta}D_{\min}\right) \quad \text{for } 0 \le T \le \bar{\theta}D_{\max}/J \tag{19}$$

$$\Omega_{Q,u}\left(S_T\right) = 1 - \left(1 - \left(1 - \sqrt{\frac{\bar{\theta}D_{\max} + \bar{\theta}D_{\min} - 2S_T}{\bar{\theta}D_{\max} - \bar{\theta}D_{\min}}}\right) \mathrm{H}\left(S_T - \bar{\theta}D_{min}\right)\right) \quad \text{for } 0 \le S_T \le \left(\bar{\theta}D_{\max} + \bar{\theta}D_{\min}\right)/2 \tag{20}$$

The SAS function in this case is zero for S_T less than $\bar{\theta}D_{min}$. It then rises increasingly steeply for $S_T > \bar{\theta}D_{min}$ until it reaches the total storage. This behavior is nearly identical to that observed in the numerical results, particularly for the steep, homogeneous case, which has the deepest water table. (More details about the condition for the linearity can be found in Supporting Information S1). Differences could be due to the non-linear variation in the water table depth (determined by Equation [11]) and unsaturated zone saturation along the hillslope.

To make more precise estimates of the storage $S_u(x)$ in the numerical simulations above we may use Equation (11) to obtain $D(x)$ and multiply this with an estimated vertically-averaged $\bar{\theta}(x)$. We can obtain $\bar{\theta}(x)$ using the one-dimensional Richards equation, Equation (1) with $i \in \{z\}$ with steady state boundary conditions of constant flux at the surface ($q = -k(\psi, z)\frac{d(\psi+z)}{dz} = J$ at $z = 0$) and constant saturation at the water table $\theta(D(x)) = \theta_s$). Unfortunately, even for one-dimensional cases, the Richards equation is hard to solve analytically with the highly non-linear van Genuchten soil water retention curve and the van Genuchten-Mualem relationship. Certain approximations on the soil water retention curve and the relative hydraulic conductivity allow us to derive an analytical solution for S_u (x; and thus T_u (x)), and the solution can be found in Supporting Information S1.

The blue dotted lines in Figure 2 show the unsaturated zone SAS function estimated using the approximate analytical solutions for $D(x)$ and $\bar{\theta}(x)$. The close matches between the analytical SAS functions and the functions estimated by ParFlow and SLIM-FAST (bold lines) confirm that $\Omega_{Q,u}$ is controlled by S_u (Kolmogolov-Smirnov distance < 0.05).

3.4. Saturated Zone Transport

Saturated zone transport is more complicated than unsaturated zone transport since the flow field is (in our idealized simulations) two-dimensional, and not a collection of parallel one-dimensional systems. However, we can simplify the two-dimensional flow and transport using Dupuit-Forchhemier assumptions and mass balance arguments.

3.4.1. General Formulation With Dupuit-Forchhemier Assumption

A useful characteristic of the saturated zone transit time problem is that it is reasonable to assume a monotonic relationship between travel time and distance upslope (Haitjema, 1995; Fiori et al., 2009). That is, the fraction of discharge leaving with a transit time in the saturated zone less than some time T_s (i.e., the fraction defined by the cumulative saturated-zone TTD $P_{Q,s}(T_s)$) is equal to the fraction of recharge entering the saturated zone downslope of a location x_0 where recharge has a transit time of exactly T_s.

Let us define a function $x_0(T_s)$, where x_0 is the x-directional location where a water particle recharged at the location has saturated zone transit time T_s. We assume that the point of origin x_0 is uniquely determined by the travel time T_s and that x_0 monotonically decreases with T_s (Fiori et al., 2009; Haitjema, 1995). With these assumptions, the transit time distribution can be written as (e.g., Haitjema, 1995):

$$P_{Q,s}\left(T_s\right) = 1 - \frac{x_0\left(T_s\right)}{L}. \tag{21}$$

The injection location x_0 associated with transit time T_s can be determined using its inverse function $T_s\left(x_0\right)$. This relationship can be found if the velocity field (specifically the component of velocity normal to the exit plane, in this case x) is known:

$$T_s(x_0) = \int_{x_0}^{L} \frac{1}{v_x(x', z_d(x', x_0))} dx' \tag{22}$$

where v_x is the x-directional component of water velocity, and $z_d(x', x_0)$ is the vertical location of a particle when its point of origin is x_0 and it has reached $x' > x_0$.

If the functions v_x and z_d can be estimated, then the TTD can be obtained by eliminating x_0 between the equations above. Under the Dupuit-Forchheimer assumptions the x-directional local velocity $v_x(x, z)$ is:

$$v_x(x, z) = -\frac{k_s(x, z)}{\theta_s} \frac{dh(x)}{dx} \tag{23}$$

where h is the hydraulic head. Note that the hydraulic head gradient does not depend on z under the Dupuit-Forchheimer assumptions. Consequently, in the homogeneous case v_x is a function of x only—Thus $v_x(x, z_d)$ in Equation (22) and $v_x(x, z)$ in Equation (23) can be replaced with $v_x(x)$. Otherwise, we can estimate z_d through mass balance by equating the rate of recharge between x_0 and x with the cumulative downslope flux between z_d and the water table height $h(x)$:

$$-\int_{z_d(x,x_0)}^{h(x)} k_s(x, z')\, dz' \frac{dh(x)}{dx} = J(x - x_0) \tag{24}$$

The right hand side term is the recharge flux between x_0 and x, and the left hand side term is the lateral flux at x along $z \in [z_d(x, x_0), h(x)]$. A similar equation can be formulated balancing the recharge between 0 and x_0 and with the flux along $z \in [0, z_d(x, x_0)]$. When the exponential decline with depth given in Equation (3) is used, $z_d(x, x_0)$ is given by:

$$z_d(x, x_0) = h(x) - P\log\left(\frac{x}{(x - x_0)\, e^{-\frac{h(x)}{P}} + x_0}\right) \tag{25}$$

Equations (21, 23) and (25) provide the TTD and the SAS function for a given water table profile $h(x)$. That profile can be estimated using the model developed in Section 3.2. While the complicated functions involved make it difficult to obtain a closed-form of the SAS function for the general case, the steps can be followed numerically. The dotted green lines in Figure 2 compare the approximate SAS functions estimated based on this model with those of ParFlow. The approximate solutions match the SAS function estimated from the Richards equation-based model. This suggests that the assumption of constant $\frac{dh}{dx}$ along a vertical profile—the Dupuit-Forchheimer assumption—is valid for estimating transport through hillslopes with and without exponentially-declining permeability. This greatly reduces the complexity of the model describing transport.

3.4.2. Approximate Analytical Solutions Using the Effective Thickness Assumption

Useful analytical solutions can be found with simplification. To obtain approximate solutions we assume an "effective" water table height, whereby water table height H_e is constant in space. Hydraulic head for the effective thickness aquifer can be estimated based on the previous mass balance argument, that is, using Equation (24) with $x_0 = 0$. The transmissivity for this case is $K_H = \int_0^{H_e} k_s(z) dz = k_0 P\left(1 - e^{-H_e/P}\right)$ and does not depend on x. Thus, the hydraulic head gradient is a linear function similar to the homogeneous case. However, resulting TTDs and SAS functions are not exponential and linear, respectively, because v_x in Equation (23) is now a function of z. The TTD and the SAS function can be estimated using Equations (21) – (25) and can be formulated as:

$$\begin{aligned} P_Q(T_s^*) &= \frac{1}{1 - \frac{1}{2}e^{-P^*}\left(1 + \coth\left(\frac{T_s^*}{2(1 - e^{P^*})}\right)\right)} \\ \Omega_Q\left(S_{T,s}^*\right) &= \frac{1}{1 - \frac{1}{2}e^{-P^*}\left(1 + \coth\left(\frac{S_{T,s}^*\left(1 + \sum_{n=2}^{\infty} \frac{S_{T,s}^{*(n-1)} \sum_{k=1}^{n-1} I_{n,j,m} e^{mP^*}}{n!\,(-1 + e^{(n-1)P^*})}\right)}{2(1 - e^{P^*})}\right)\right)} \end{aligned} \tag{26}$$

where $l_{n,j,m} = \sum_{j=0}^{m-1} \binom{n}{j} (-1)^j (m-j)^{n-1}$. To simplify the equations the saturated zone age-ranked storage $S_{T,s}$ and transit times T_s are expressed in dimensionless forms $S^*_{T,s} = \frac{S_{T,s}}{P\theta_s}$ and $T^*_s = J\frac{T_s}{P\theta_s}$, respectively. $S_{T,s}$ ranges between 0 and $H_e\theta_s$. Note that the SAS function does not depend on J, only on the storage.

The thick light gray lines in Figure 2 show the analytically derived SAS function using Equation (26) for the considered cases. For the homogeneous hillslope, the analytical solutions were illustrated for the upper half; we will discuss the reason why in the following section. The thickness of the effective aquifer H_e was determined as the spatial average of h, denoted as $\bar{h}$ hereafter, for each case. The model worked for all the cases effectively with the maximum Kolmogorov-Smirnov distance of 0.06 for the case with $P = 2.0$ and $\tan\beta = 0.15$. Detailed reasons why the effective thickness assumption-based model works are described in Supporting material S2.

Moreover, the agreement implies that the role of the no-flow condition in the saturated zone boundary condition at the most downslope (that used in the PARFLOW model) is negligible for the cases considered in this study. A detailed examination of the effect of the boundary conditions is out of the scope of this study. Nevertheless, previous work has shown that the extent of the no-flow condition at the lower boundary has a negligible effect on the system-scale transport (for the homogeneous semi-confined aquifer) when $H_e/L < 0.1$ (Luther & Haitjema, 1998). Our results indicate that H_e in the condition may need to be replaced with the active saturated zone thickness (in terms of transport) when the permeability declines along the depth.

As the effective thickness model works in many cases, it would be worthwhile to look at limiting cases to see if we can simplify the analytical solution. We can define two limiting cases: $P \to \infty$ and $H_e \to \infty$. When $P \to \infty$, the aquifer is homogeneous. The case $H_e \to \infty$ can be thought of as the case when the decline length scale P is very small compared to H_e. (The latter condition is similar to the condition of large $P^* = H_e/P$, which will be discussed later.) For these cases, the TTDs can be written as:

$$\begin{aligned} P_Q(T^*) &= 1 - e^{-T^*} \qquad (\text{when } P \to \infty) \\ &= \frac{T^*}{1+T^*} \qquad (\text{when } H_e \to \infty) \end{aligned} \tag{27}$$

where $T^* = \frac{JT_s}{H_e\theta_s}$ for $P \to \infty$ and $T^* = \frac{JT_s}{P\theta_s}$ for $H_e \to \infty$.

As previously discussed, the transit time distribution for the homogeneous aquifer ($P \to \infty$) is exponential and identical to Equation (7). For the case which the saturated conductivity declines much faster than the aquifer thickness, the TTD is a Lomax distribution (Johnson et al., 1994, 1995) with exponent 1. The associated SAS functions are:

$$\begin{aligned} \Omega_Q\left(S^*_{T,s}\right) &= S^*_{T,s} \qquad (\text{when } P \to \infty) \\ &= 1 - e^{-S^*_{T,s}} \qquad (\text{when } H_e \to \infty) \end{aligned} \tag{28}$$

where $S^*_{T,s} = \frac{S_{T,s}}{H_e\theta_s} \in [0,1]$ for $P \to \infty$ and $S^*_T = \frac{S_{T,s}}{P\theta_s} \in [0,\infty)$ for $H_e \to \infty$.

The solutions for $H_e \to \infty$ are a reasonable approximation when, roughly, $P^* > 5$. For $P^* > 5$, the analytical solution in Equation (26) differs from the exponential SAS function above with the maximum Kolmogolov-Smirnov distance of less than 0.007. For the hillslopes with $P = 0.5$ and the case of $\{P = 2.0, \tan\beta = 0.30\}$, the SAS function is approximately exponential as $P^* > 5$ with $H_e = \bar{h}$ (see Figure 2).

The derived saturated zone TTDs and the SAS function can be used to estimate the hillslope scale TTD and SAS function in Section 3.5. Furthermore, those solutions allow us to easily examine those properties. For example, the derived saturated zone TTD is heavy-tailed but not 1/f scaled, which is discussed in the following section.

3.4.3. Heavy-Tailed (But Not 1/f Scaled) Transit Time Distribution Through the Saturated Zone

The analytical derivations of the TTDs, Equations (26) and (27), allow us to look at those statistical properties easily. Our two particular interests are its tailing and power spectrum. The tailing of TTD has been studied and used to characterize transport at a scale of interest. The power spectrum of the TTD has served as a useful tool to understand catchment-scale transport, for example, in Kirchner et al. (2000) and Godsey et al. (2010).

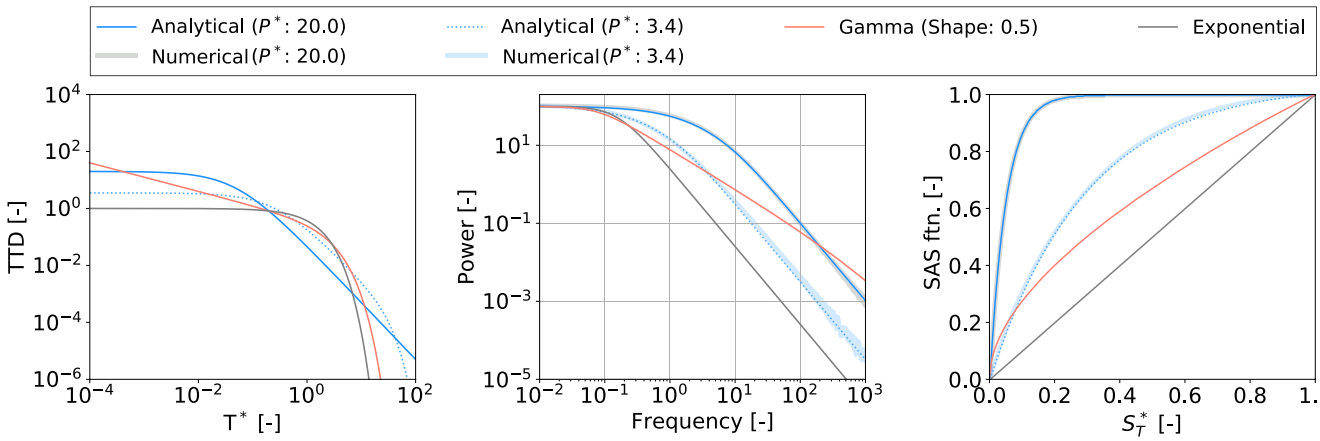

Figure 6. The saturated zone transit time distributions, those power spectrum, and the StorAge Selection functions.

As described previously, Ameli et al. (2016) reported that the numerically estimated TTD for $P \approx 0.3$ m (or $\bar{h}/P \approx 3.4$) can be fitted to the gamma distribution with the shape factor of 0.5, which is associated with the 1/f scaling (Kirchner et al., 2000).

The analytical TTD is heavy-tailed when $P^* < \infty$. (Heavy-tailed distribution refers to the distribution whose tail is not bounded exponentially (Bryson, 1974).) This heavy-tailed distribution suggests that if one treats the hillslope as an effective one-dimensional system (similar to the way used in Kirchner et al., [2001]) the system-scale transport is non-Fickian. The exponential decline in the saturated hydraulic conductivity results in non-Fickian behavior despite lacking a stochastic hydraulic conductivity field or dual-domain model assumptions.

In addition, the TTD in Equation (26) does not show the 1/f scaling (see the middle panel of Figure 6). Gamma distribution with its shape factor 0.5 has the 1/f signal, because $T \sim \Gamma\left(\frac{1}{2}, T_m\right)$ decays following $T^{-0.5}$ up to around the mean transit time T_m. However, the TTDs in Equations (26) and (27) do not have such regions (see the left panel in Figure 6). Nevertheless, if we "fit" a gamma distribution to the TTD by minimizing, for example, mean squared error, the gamma distribution with the shape factor $\alpha = 0.5$ is the best fit for the case of $P^* = 3.4$, because the gamma distribution can reproduce the heavy-tailed TTD with $\alpha < 1$. Thus, it is likely that the TTDs at these hillslopes do not have the $1/f$ characteristic, and the result in the previous study is an artifact of such fitting. While we only looked at this property for the saturated zone transport, it is unlikely that the unsaturated zone transport endows $1/f$ scaling, especially when P is low.

3.5. Hillslope Scale Transport

Hillslope scale transit time T can be formulated as the sum of the unsaturated zone transit time T_u and the saturated zone transit time T_s as: $T = T_u + T_s$. Following our previous discussion, T_u, T_s, and T may be determined by the associated injection location of water particle x_0. Thus, it is possible to formulate hillslope scale transit time distribution $P_Q(T)$ using Equation (14) by replacing T_u with $T_u + T_s$. In case T is a monotonically decreasing function of x_0, Equation (21) may be used to estimate the hillslope scale transit time distribution by replacing T_s with $T_u + T_s$. The SAS function can be constructed using the transit time distribution.

We also can ask another question: can we construct hillslope scale TTD and SAS function using those of unsaturated zone and saturated zone? This question is directly related to the problem of determining a system-scale transport measure, where the system is composed of multiple sub-systems (or buckets) in a series and when we know about sub-system scale transport closures (either TTDs or the SAS functions). Unfortunately, it is not possible unless we have additional information on a certain relationship between T_u and T_s.

In the theory of probability, a probability distribution of the sum of two continuous random variables, let's say $T = T_u + T_s$, can be formulated as (e.g., Wackerly et al., 2002):

$$p_Q(T) = \int_0^T p_{Q,u,s}(\tau, T-\tau)d\tau \tag{29}$$

where $P_{Q,u,s}(T_u, T_s)$ is the joint distribution of T_u and T_s.

Thus, we need to know the joint distribution, not $P_{Q,u}$ and $P_{Q,s}$, to determine the hillslope scale transit time distribution. Determining the joint distribution using only $P_{Q,u}$ and $P_{Q,s}$ is, in general, not possible. Those are marginal distributions of the joint distribution which can be formulated as: $P_{Q,u}(T) = \int_0^T \int_0^\infty p_{Q,u,s}(\tau,\eta)d\eta d\tau$, and $P_{Q,s}(T) = \int_0^T \int_0^\infty p_{Q,u,s}(\eta,\tau)d\eta d\tau$. Through the integration some information in $p_{Q,u,s}$ is destroyed and cannot be recovered using $P_{Q,u}$ and $P_{Q,s}$.

Nevertheless, we can think of two end-member cases where determining the joint distribution is possible using $P_{Q,u}$ and $P_{Q,s}$. First, the determination is possible when the two random variables T_u and T_s are independent; in such case, the joint distribution is multiple of the two: $p_{Q,u,s}(T_u, T_s) = p_{Q,u}(T_u)p_{Q,s}(T_s)$, and Equation (29) reduces to the convolution: $p_Q(T) = \int_0^T p_{Q,u}(\tau)p_{Q,s}(T-\tau)d\tau$ (e.g., Hogg et al., 2005). This is useful, for example, when the unsaturated zone transit time is mostly constant as $T_u(x_0) \approx T_1$ for all $x_0 \in (0, L]$ where T_1 is a constant. In this case, $p_{Q,u}(T_u) = \delta(T_u - T_1)$, where δ is Dirac-delta function, and $p_Q(T)$ is simply equivalent to $p_{Q,s}(T - T_1)$ for $T \geq T_1$. Otherwise $p_Q(T) = 0$. If we further assume that the saturated zone is homogeneous and water table gradient is negligible, the assumptions yields the "piston-exponential" function as the hillslope scale transit time distribution (Małoszewski & Zuber, 1982). The function has been used widely, especially, in tritium dating (e.g., Morgenstern et al., 2010; Zuber et al., 2005). Generalization is possible using Equation (26), or Equation (27), to consider the effect of the exponential hydraulic conductivity decline with depth. For the case of $H_e \to \infty$, the hillslope scale TTD is a piston-Lomax(1,1) like distribution or, more formally, the generalized Pareto distribution with ($\mu = T_u/T^*$, $\sigma = 1$, $\eta = 1$) (Pickands, 1975), when the same normalization used for Equation (27) is applied.

On the other hand, T_u and T_s are maybe not independent of each other but related by a single-valued function q as: $T_s = q(T_u)$. Let us assume that q is any monotonically increasing function. Then there exists a strictly increasing function w that satisfies $T = w(T_u) = T_u + T_s = T_u + q(T_u)$. In this case, the TTDs are related by $P_{Q,u}(T_u) = P_{Q,s}(T_s = q(T_u)) = P_Q(T = w(T_u))$. These give an interesting relationship between the age-ranked storages, S_T, $S_{T,u}$, and $S_{T,s}$, as:

$$\begin{aligned} S_T(T) &= J\left(T - \int_0^T P_Q(\tau)d\tau\right) = J\left(w(T_u) - \int_0^{w(T_u)} P_Q(\tau)d\tau\right) \\ &= J\left(T_u + q(T_u) - \left(\int_0^{T_u} P_{Q,u}(\tau)d\tau + \int_0^{q(T_u)} P_{Q,s}(\tau)d\tau\right)\right) \\ &= S_{T,u}\left(w^{-1}(T)\right) + S_{T,s}\left(q\left(w^{-1}(T)\right)\right) \end{aligned} \tag{30}$$

where w^{-1} is the inverse function of w and it exists since w is strictly increasing function. For the equation in the second line we used the relationships: $dw(T_u) = dT_u + dq(T_u)$ and the previously mentioned relationship between the TTDs.

The above Equation (30) means that the age-ranked storage for the whole hillslope is the sum of the unsaturated age-ranked storage and the saturated age-ranked storage when the value of the SAS functions are the same: $S_T(\Omega_Q) = S_{T,u}(\Omega_Q) + S_{T,s}(\Omega_Q)$. In other words, the SAS for the hillslope as a whole is the sum of the unsaturated and saturated SAS functions if we rotate the SAS function plot counter-clockwise 90°. The assumption of the monotonic increasing function q is valid for several cases that are considered here because the water table gradient is usually lower than the surface slope. The validity can be easily checked using Equation (3) in Supporting Information that estimates $S_u(x)$. If S_u (and thus T_u) is one-to-one on x, the monotonic increase is valid. Finally, the black dotted lines in Figure 2 illustrate the hillslope scale SAS functions that are estimated using the method described in this section, which is very close to those estimated by ParFlow and SLIM-FAST (bold dark gray lines in Figure 2).

3.6. Internal Age, Life Expectancy, and Transit Time Structures

In this section we described the internal age, life expectancy, and transit time structures using the previously developed models. The numerical results were introduced previously and illustrated in Figure 3. The model for the velocity field, Equations (23)–(25), can be used to estimate the spatial age and life expectancy in saturated zone with:

$$A(x,z) = \int_{x_0(x,z)}^{x} \frac{1}{v_x\left(x', z_d\left(x', x_0(x,z)\right)\right)} dx'$$
$$LE(x,z) = \int_{x}^{L} \frac{1}{v_x\left(x', z_d\left(x', x_0(x,z)\right)\right)} dx' \tag{31}$$

Those are, again, only a function of v_x because of the Dupuit-Forchheimer assumption. For the effective thickness aquifer, using the velocity field that discussed in Section 3.4.2, the above can be written analytically as:

$$A(z) = \frac{P\theta_s\left(e^{H_e/P}-1\right)}{J}\log\left(\frac{1-e^{-H_e/P}}{1-e^{-z/P}}\right)$$
$$LE(x,z) = \frac{P\theta_s\left(e^{H_e/P}-1\right)}{J}\log\left(1+e^{-z/P}\left(\frac{L}{x}-1\right)\right) \tag{32}$$

For the effective thickness aquifer the age-structure is not a function of x and only a function of z, while the life expectancy is a function of x and z unless the hydraulic conductivity is homogeneous; when, $P \to \infty$, $LE(x) = \frac{H_e\theta_s}{J}\log\left(\frac{L}{x}\right)$. (In that case, $A(z) = \frac{H_e\theta_s}{J}\log\left(\frac{H_e}{z}\right)$ (e.g., Cornaton & Perrochet, 2006; Raats, 1978; Vogel, 1966). The independency of the age structure on z means that the structure is parallel to the surface and impermeable layer of the effective thickness aquifer. As we talked about previously, the effective thickness assumption was valid for certain cases to explain the transport closures in unconfined aquifers. From the success, we can expect that the model Equation (32) would also be valid to explain the age and life expectancy structures. However, it is not clear how to map the findings from the effective thickness aquifer to the unconfined aquifers as h varies in the latter case. Is it a water table or impermeable layer that the parallel age structure referenced to?

The question could be answered, if we can find analytical expressions for Equation (31), by examining those functional forms. However, analytical forms of Equation (31) are hard to be obtained, and we thus took another way and focused our discussion on the two limiting cases: $P \to \infty$ and $h \to \infty$. Let us first define $d_d(x, x_0) = h(x) - z_d(x, x_0)$ as the depth from the water table where a water particle injected at x_0 is located at x. (z_d was formulated in Equation (25), and we shall use $h_2(x)$ in Supporting Information S3 as $h(x)$ for the upslope half of homogeneous aquifer in this discussion when $P \to \infty$.) If an age structure parallels to the water table appears, we should be able to formulate d_d with A not x nor x_0. Let us also define new variable $x_A(A, x_0)$ as the horizontal location of a water particle injected at x_0 at age A, which can be formulated by inversing $A(x_A, x_0) = \int_{x_0}^{x_A} 1/v_x(x')\,dx'$. Using x_A, d_d can be written as:

$$\begin{aligned} d_d\left(x_A(A,x_0), x_0\right) &= -P\log\left(1-\left(1-\frac{x_0}{x_A(A,x_0)}\right)\left(1-e^{-h\left(x_A(A,x_0)\right)/P}\right)\right) \\ &= h\left(x_A(A,x_0)\right)\left(1-\frac{x_0}{x_A(A,x_0)}\right) \qquad (\text{when } P\to\infty) \\ &= -P\log\left(\frac{x_0}{x_A(A,x_0)}\right) \qquad (\text{when } h\to\infty) \end{aligned} \tag{33}$$

For the limiting cases, analytical formulations of x_A/x_0 are possible by inversing $A(x_A, x_0)$ as:

$$\begin{aligned} \frac{x_0}{x_A(A,x_0)} &= e^{-aA} \qquad (\text{when } P\to\infty) \\ &= \frac{1}{1+bA} \qquad (\text{when } h\to\infty) \end{aligned} \tag{34}$$

where $a = \frac{J}{\theta_s h_0}$, $h_0 = \sqrt{h_L^2 + \frac{JL^2}{k_s}}$ is the water table height at $x = 0$, and $b = \frac{J}{P\theta_s}$.

These allow us to examine the age-structure for the limiting cases by replacing $x_0/x_A(A, x_0)$ in Equation (33) by Equation (34). For the upper half of the homogeneous aquifer (when $P \to \infty$), d_d/h is a function of A not x and x_0. This means that the age-structure is not parallel to either the impermeable layer or the water table but to the

normalized coordinate z/h or d/h. This case is identical to the type of spatial age distribution called "scaled lateral symmetry" in Harman and Kim (2019). For the case $h \to \infty$, d_d is a function of A not x and x_0. This means that the age-structure is parallel to the water table. These age structures can be written as:

$$A(d_n) = \frac{1}{a}\log\left(\frac{1}{1-d_n}\right) \qquad \text{(when } P \to \infty\text{)}$$
$$A(d) = \frac{1}{b}\left(e^{\frac{d}{P}} - 1\right) \qquad \text{(when } h \to \infty\text{)} \tag{35}$$

where $d_n = d/h$.

This shows how the depth-independence of age-structure in the effective thickness (or semi-confined) aquifers is reflected in the unconfined aquifers for the limiting cases. Using the above results, we can classify two regimes of age-structure: "lateral symmetry" (Harman & Kim, 2019) and "water table parallel". The structure $A(d_n)$ presented above has the identical functional form to that for the homogeneous effective thickness aquifer when d_n replaces with d/H_e or $1 - z/H_e$ (see the equation below (32)). The rates are a little different from each other as the effective thickness H_e is replaced with h_0 for the upslope half of the unconfined Boussinesq aquifer. The "water table parallel" regime appears when, roughly, $P^* > 5$. In the literature, the water table parallel regime has also appeared for the case where the water table thickened linearly from upslope to downslope (e.g., Cook & Böhlke, 2000). (Note that the water table is more or less thinning linearly for the case considered here.) While the structure is similar in the two cases, the rate that the age increases with depth is different significantly. It is linear with the rate of $\frac{\theta_s}{J}$ for the linear thickening case (Cook & Böhlke, 2000) and is exponential for the exponential decline of saturated hydraulic conductivity cases.

The upper three panels in Figure 7 shows the saturated zone age-structures estimated using Equation (32) for the cases with $\tan\beta = 0.15$ and three different P values. In the homogeneous aquifer, the structure is linear for the upslope half in d_n co-ordinate. For $P = 0.5$ $\left(P^* = \bar{h}/P = 15.6\right)$, the age structure is parallel to the water table which can be seen easily in d co-ordinate. For $P = 2.0$ $\left(P^* = \bar{h}/P = 2.73\right)$, the structure cannot be explained by the two limiting cases.

The structure can be altered when we consider the time water spent in the unsaturated zone as we can see in the second row of Figure 3. Thus, the above discussion is valid for the hillslope as a whole for the cases where unsaturated zone transit time $T_u(x)$ is mostly constant along x. When this is not true, the age structure is different from what is discussed in this section. Examining such cases ($T_u(x) \neq$ const.) in a simple manner would also be possible using: $A(x_A, x_0) = \int_{x_0}^{x_A} 1/v_x(x')dx + T_u(x_0)$. However, this is out of the scope of this paper, and we leave it as a future study.

In terms of the life expectancy structures, those vary mostly depending on P. The contour lines of the life expectancy are orthogonal to the impermeable layer for the case $P \to \infty$, as the horizontal velocity of water particles along a vertical line is constant under the Dupuit-Forchheimer assumption. This is also approximately true in the Richards equation-based model (see the top-left panel in Figure 3). In fact, the life expectancy structures for the saturated zone are mostly identical to those estimated at the hillslope as a whole (in Figure 3), since life expectancy is determined from the outlet. As a result, the effect of P on the structure is the same as discussed previously for the hillslope as a whole; low P results in tilting the contour lines as the lateral velocity is slower at more bottom locations.

The saturated zone transit time structure can also be obtained using Equation (31) as $T(x, z) = A(x, z) + LE(x, z)$, and the structures are illustrated in the bottom panels of Figure 7. The structures for the hillslope as a whole are shown in Figure 3. As previously described, the contour lines of the transit time structure illustrate the flow pathways under steady state. The flow pathways were determined more by the surface topography when P is smaller as those are mostly parallel to the soil surface. Moreover, the contour lines showed that, when P is small, most of the recharged water moves through a very shallow layer underneath the water table, and the water below the layer was water recharged at the very narrow upslope locations.

3.7. Correlated Hi_X, P^*, and Unsaturated Zone Transit Time

Throughout this study, we defined several dimensionless numbers such as Hi_X and P^*. Hi_X and P^* explain saturated zone flow and transport, respectively. The exponential Hillslope number Hi_X is similar to the Hillslope number $Hi = \frac{L\tan\eta}{2\bar{H}}$ (Brutsaert, 1994). The effective thickness $\bar{H}$ is substituted with P in Hi_X, and the slope of

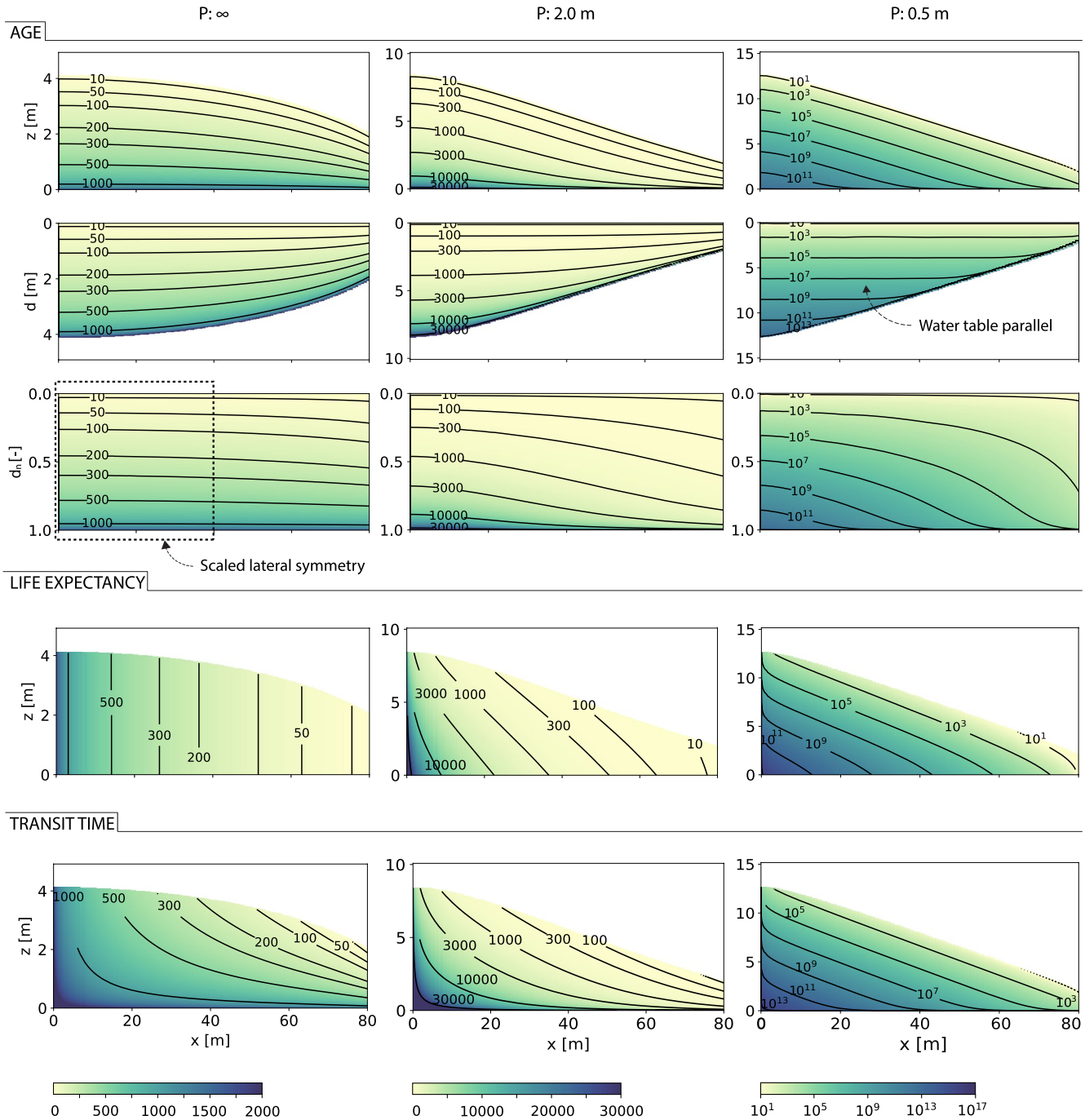

Figure 7. Age, life expectancy, and transit time structures in the saturated zone for different P with $\tan\beta = 0.15$. The age structures are illustrated in three vertical coordinates: the height above the impermeable layer z, $d = h - z$, where h is water table height, and $d_n = d/h$. The life expectancy and the transit time structures are illustrated in z coordinate.

the impermeable base is replaced with the surface slope. P^* is the number that determines the saturated zone transport.

The two numbers, Hi_X and P^*, are correlated: Hi_X determines the water table profile with M, $\hat{H}_t$, and $\hat{H}_L$, and P^* is proportional to the (average) water table height. The upper panels in Figure 8 illustrate P^* as a function of Hi_X and M for several selected H_ts. The figures show that the saturated zone transport number P^* is largely determined by Hi_X rather than M. With that in mind, this is perhaps worthwhile to note here that, roughly, $P^* > 5$

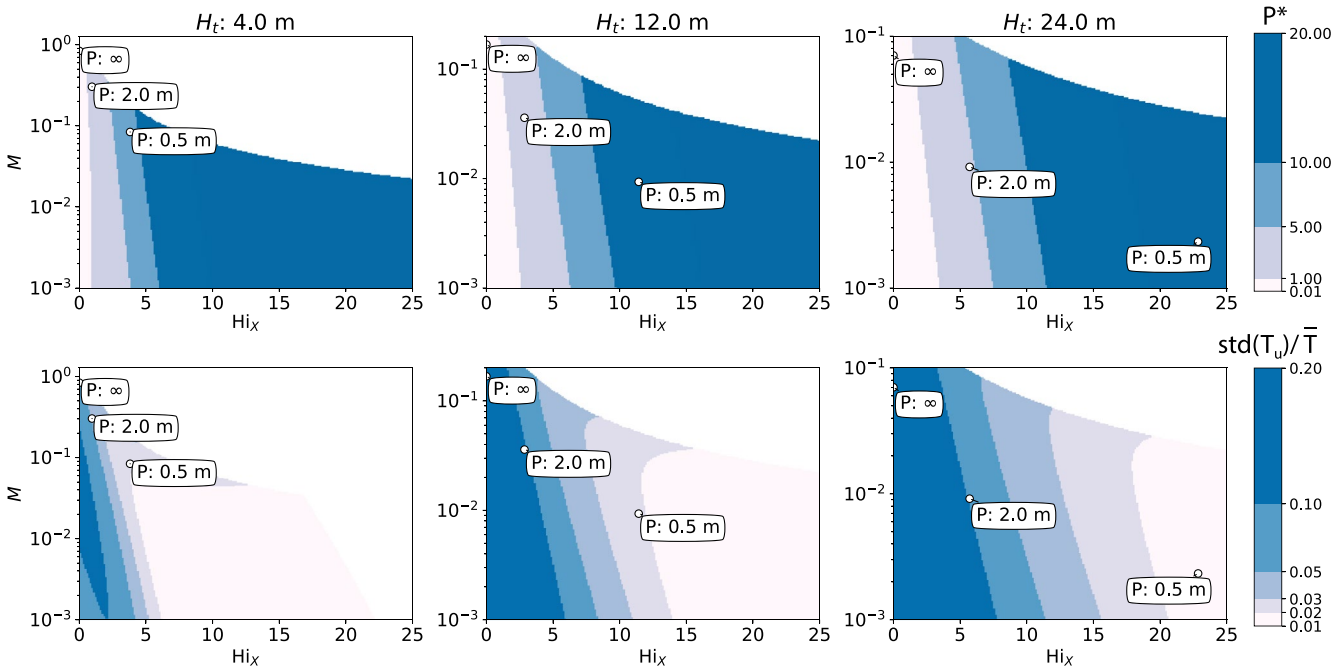

Figure 8. (Top) The saturated zone transport number P^* $\left(=\bar{h}/P\right)$ as a function of M $(=J/(k_0(\tan\beta)^2))$ and the exponential Hillslope number Hi_X. In the above equations, $\bar{h}$ is the average of water table height, P is the decline length scale, J is the steady rain rate, k_0 is the saturated hydraulic conductivity at the soil surface, and β is slope of the surface. (bottom) the ratio of the standard deviation of unsaturated zone transit time $T_u(x)$ to the mean hillslope transit time $\bar{T}$. The location of the nine dots indicates the nine considered cases.

when $\mathrm{Hi}_X > 10$. The condition of $\mathrm{Hi}_X > 10$ is the condition that TOPMODEL works (see Figure A1). This means that the SAS function associated with TOPMODEL is an exponential function for two-dimensional hillslopes.

The exponential Hillslope number Hi_X is also related to the unsaturated zone transport. One of its important controls is the effect on the variance of the unsaturated zone transit time $T_u(x)$ for $x \in [0, L]$. The variance (or standard deviation) of the unsaturated zone transit time is important as it can be used as a measure of determining the method to combine the unsaturated and the saturated TTDs and the SAS functions (as discussed in Section 3.5). Also, it determines the validity of the discussion on the saturated zone age structure, presented in Section 3.6. As we can expect from Figure 5, the higher the Hi_X the smaller the standard deviation, because the water table is largely determined by the topographic surface when Hi_X is high. The bottom panels of Figure 8 show the ratio of the standard deviation of T_u to the mean hillslope transit time $\bar{T}$, as a function of Hi_X and M. As it was expected, the standard deviation was largely determined by Hi_X. When $\mathrm{Hi}_X > 10$, the ratio was, roughly, less than 0.1 for the considered cases.

4. Application and Limitations

In this section, we evaluate the theoretical framework in terms of estimating the SAS function and the tracer breakthrough curve (BTC) in two experimental hillslopes. The two experimental systems have quite distinct Hillslope numbers Hi. For one system, we will consider the exponential decline in the saturated hydraulic conductivity with depth. We will also discuss the limitations of the current framework that the application highlights.

The two experimental systems are (a) one of the Landscape Evolution Observatory (LEO) hillslopes, the LEO west hillslope, located in Biosphere 2, The University of Arizona (with a Hillslope Number of Hi > 10), and (b) a small-scale sloping soil lysimeter called *miniLEO* located in the same facility (with Hi ≈ 0.2). The LEO west hillslope is 30 m long, 11 m wide, and 1 m deep hillslope supported by a steep and convergent plan shape steel structure (e.g., Pangle et al., 2015). MiniLEO is a smaller scale experimental system which is 2 m long, 0.5 m wide, and 1 m deep (e.g, Kim et al., 2016). It is supported by a straight planar steel base. The average slope of

both LEO west and miniLEO is 10°. Both of the experimental systems are primarily filled with a loamy-sand textured basaltic tephra except for the downslope region (0.5 m long for the LEO west hillslope and 0.1 m long for miniLEO) where gravel textured basaltic tephra is filled. The porosity of the loamy-sand textured soil is approximately 0.4. The saturated hydraulic conductivity for both systems was estimated in previous studies. The hydraulic conductivity of the LEO west hillslope is effectively homogeneous and is about 10 m/day (e.g., van den Heuvel et al., 2018). For miniLEO it is about 0.3–3.5 m/day, and is highest in topsoil and decreases with depth (Pangle et al., 2017).

Tracer datasets and the observed SAS functions are available for experiments conducted on both systems. A tracer experiment conducted in 2016 at the LEO west hillslope produced tracer BTCs and the observation of the SAS functions (Kim, Volkmann, et al., 2022). For miniLEO, we use the data collected during the 2014 experiment and the observed SAS functions reported in (Kim et al., 2016). Both experiments used the PERiodic Tracer Hierarchy (PERTH) method (Harman & Kim, 2014) to observe the SAS function at periodic steady state (see Figures 9 and 10). Both systems were driven almost to the wettest possible state given the constraint that they do not generate overland flow. There is a significant difference between the two experiments in terms of Hi, which is higher than 10 in the LEO west hillslope, and it is about 0.2 in the miniLEO. The Hillslope number is determined by the average height that the water must flow $L\tan\eta/2$ and the effective thickness of the water table $\bar{H}$ as: $L\tan\eta/\left(2\bar{H}\right)$. In the LEO west hillslope, the height $L\tan\eta/2$ is on average about 2.6 m, while it is about 0.1 m in miniLEO. We use the average water table thickness during the experiments as the effective thickness $\bar{H}$ when estimating the hillslope number. The water table in the LEO west hillslope along the center is the thickest downslope with the temporal average of 0.42 and 0.47 m at 1.0 and 7.0 m upslope from the downslope boundary (Kim, Volkmann, et al., 2022). It decreases toward the upslope, and no water table was developed at the most upslope region. The spatial and temporal average thickness is less than 0.3 m. In miniLEO, the water table extended up to the upslope boundary, with time-averaged thicknesses of 0.49 m, 0.53 m, and 0.39 m at 0.15 m, 0.75 m, and 1.35 m from the downslope boundary, respectively. The spatial and temporal average thickness was 0.45 m (Kim et al., 2016).

The observed SAS functions in each system differ greatly from one another (see Figures 9 and 10b). The shape of the observed SAS function in the LEO west hillslope is concave, indicating the preferential discharge of old water (Kim, Volkmann, et al., 2022). The SAS function mainly shifts to the right as the system becomes wetter, meaning that the hillslope preferentially discharges older water from storage under wetter conditions. In contrast, the SAS function observed in miniLEO indicates that the system preferentially discharges younger water storage during wetter conditions. The phenomenon in which young water is released in greater proportion under wetter conditions is termed “inverse storage effect” (Harman, 2015), and observed in many catchments (e.g., Harman, 2015; van der Velde et al., 2014). The shape of the SAS function is mostly convex except for the function over the young water storage where the shape is concave. The concave part extends as the system becomes drier.

We can compare the predictions of the theory developed above with the observed SAS functions and the observed BTCs. For the LEO west hillslope where Hi is high, an analytical solution of the steady state SAS function is provided based on the framework that we described in the proceeding sections and by utilizing the kinematic wave assumption. They estimated the water table profile using the hillslope-storage kinematic wave model (Troch et al., 2002) to consider the convergent topography and estimated the SAS function using the framework provided in this study. The mean discharge is used as the steady state flux. For miniLEO, we estimate a hydraulic theory-based steady state SAS function using the effective thickness assumption discussed in Section 3.4.2, where the water table height is approximated by an effective water table height. When the unsaturated zone volume and the saturated zone volume are available, we can estimate the SAS function using those volumes and P^*. The SAS function for the saturated zone can be estimated using Equation (26). Note that, in the SAS function, the soil porosity θ_s only linearly scale the age-ranked storage; Thus, when the saturated zone storage volume is available, the value of porosity does not need to be determined, and we can linearly scale the SAS function so that the age-ranked storage at $\Omega_Q = 1$ matches the saturated zone storage. We assume the piston flow for the unsaturated zone volume, and the hillslope scale SAS function is the saturated zone SAS function shifted by the amount of the unsaturated zone. We estimate the storage volumes using the water table data measured at the three locations and the soil water content data measured at 15 locations (Kim et al., 2016). The region under the water table and the region above the water table up to the extent of the tension saturated zone (0.2 m; see Pangle et al. [2017]) was treated as the saturated zone and the storage volume was estimated using the soil water content data. The unsaturated zone storage was also estimated using the soil water content data above the saturated zone. The

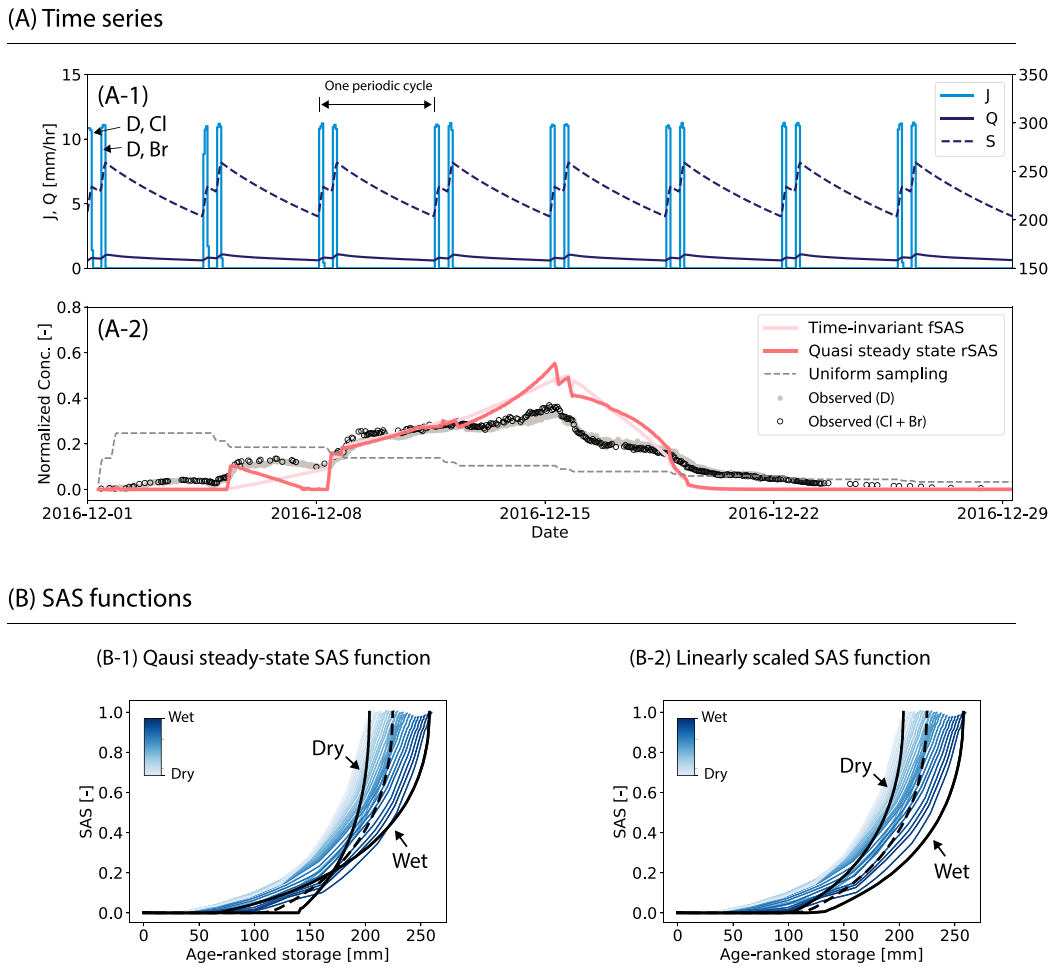

Figure 9. (a) Time series of the experiment conducted at the landscape evolutionary observatory (LEO) west hillslope. (A-1) The effective rainfall, discharge, and storage. Deuterium, Cl^-, and Br^- were used as a tracer, and the pulses that are labeled with those tracers are indicated in this plot. (A-2) The observed and the simulated breakthroughs. (b) The StorAge Selection (SAS) functions. The observed SAS functions are illustrated by the blue lines. The color saturation indicates the storage state from wet to dry (from less saturated to more saturated; Modified from Kim, Volkmann, et al. [2022]). Note that the system is in the periodic steady state, and the SAS function during one periodic cycle is shown in the figure. The dotted black line illustrates the steady state SAS function estimated using the mean discharge. The bold black lines in (B-1) and (B-2) illustrate the quasi-steady state SAS functions and the linearly scaled SAS function, respectively, at the driest and the wettest conditions.

discharge weighted storage of the unsaturated zone and the saturated zone is used for the steady state. Regarding the parameter describing the decline in conductivity with depth, P^*, we consider two cases. First, we assume that there is no decline of the saturated hydraulic conductivity with depth (i.e., $P \to \infty$) and the saturated zone SAS function for this case is linear as in Equation (28); Second, we use the declining hydraulic conductivity with depth that approximates the decline used in the previous modeling study of Pangle et al. (2017) (see Figures 10b–3). In the following, we briefly discuss the SAS functions obtained experimentally and those estimated using the theory developed in this paper. This discussion is followed by a discussion of how the steady state SAS functions can be adapted to account for time-variability and used to model BTCs under time-variable conditions.

The hydraulic theory-based steady state SAS functions well approximate the observed SAS functions. In the LEO west hillslope, the concave shape of the hydraulic theory-based steady state SAS function is attributed to the high Hi and the convergent topography of the hillslope (Kim, Volkmann, Bugaj, et al., 2021; Kim, Volkmann, et al., 2022). For miniLEO where Hi is low, the case with $P \to \infty$ well approximates the observed SAS function but with a linear shape. The SAS function with $P = 1.0$ m reproduces the convexity of the SAS function

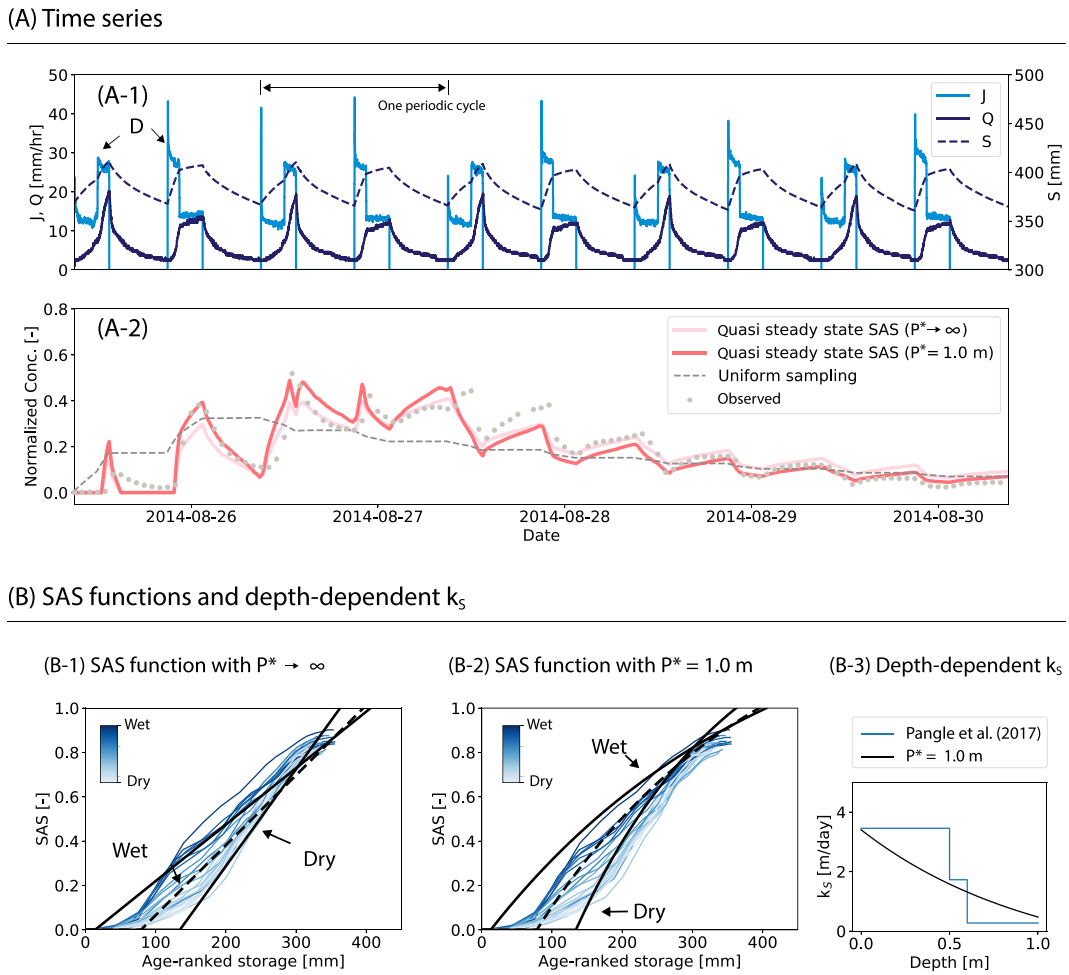

Figure 10. (a) Time series of the experiment conducted at miniLEO. (A-1) The effective rainfall, discharge, and storage. Deuterium was used as a tracer, and the pulses that are labeled with the tracer are indicated in this plot. (A-2) The observed and the simulated breakthrough curves. (b) The StorAge Selection (SAS) functions and the depth-dependent k_s. The observed SAS functions are illustrated by the blue lines. In (B-1) and (B-2), the color saturation indicates the storage state from wet to dry (from less saturated to more saturated; Modified from Kim et al. [2016]). Note that the system is in the periodic steady state, and the SAS function during one periodic cycle is shown in the figure. The dotted black line illustrates the steady state SAS function estimated using the discharge weighted storage. The bold black lines in (B-1) and (B-2) illustrate the quasi-steady state SAS functions for the case of $P^* \rightarrow \infty$ and $P^* = 1.0$ m, respectively, at the driest and the wettest conditions. (B-3) illustrates the depth-dependent k_s used in Pangle et al. (2017) and the vertical structure with $P^* = 1.0$ m.

observed at the wet conditions across most of the age-ranked storage and at the dry condition for the older water storage.

Utilizing the steady state SAS function to reproduce the BTCs observed under the unsteady state requires an additional step: how to reconcile the steady state SAS function with the time-variability of the system. There are several ways this can be done.

1. The steady state SAS function can be directly applied, assuming time-invariant flow pathways with fixed effective storage
2. he steady state SAS function can be scaled linearly each time to match the storage. This is equivalent to a time-invariant fractional SAS (fSAS) function (much like van der Velde et al. [2014])
3. We can estimate a SAS function at each time step using a quasi-steady state (QSS) assumption (where an unsteady process is approximated as a succession of steady state processes (e.g., Akylas et al., 2015; Verhoest & Troch, 2000). Either the discharge or storage time series can be used to determine the 'state' at each time

step – each will likely produce different results, and the difference will be larger when the QSS is a poor approximation

In this study, we use the storage time series to model the QSS and generate corresponding SAS functions at each time. For the LEO west hillslope, we utilize the total storage to represent the state. When calculating the SAS function at each time step, the steady state flux is chosen so that the total storage estimated by hydraulic theory matched the observed total storage in LEO west. For the time-invariant fSAS model, the estimated steady state SAS function is linearly scaled to match the observed total storage at each time step. For miniLEO, total storage is the sum of the unsaturated zone storage and the saturated zone storage. The SAS function for each zone is scaled to match the corresponding storage; As we discussed previously, both SAS functions linearly depend on the corresponding storage. Thus, when we estimate the SAS functions for each zone, there is no difference between the time-invariant SAS function application and the QSS application. Although these methods should be investigated further in detail, we will briefly compare these methods and discusses their limitations.

The hydraulic theory-based SAS function as a time-invariant fSAS function captures the observed SAS function reasonably well for the LEO west hillslope (Figures 9b–2). The quasi-steady state (QSS) hydraulic theory-based SAS function is more similar to the observed SAS function under wetter conditions (Figures 9b–1). However, the QSS SAS function shows the inverse storage effect in young water ($\lessapprox$ 170 mm of the age-ranked storage), which is not observed in this hillslope.

The simulated BTCs using those SAS functions generally follow the observed BTCs with some notable differences (Figures 9a–2). The simulated BTCs are lower than the observed BTCs during the first two cycles since the estimated SAS functions export a smaller fraction of young water compared to the observed SAS function. For the same reason, the simulated BTCs are higher than the observed BTC during the fourth and the fifth cycles, when the tracer-labeled water is old. The effect of the SAS function time-variability on the modeled BTC can best be seen during the flow recession period in the second cycle. The concentration simulated using the QSS SAS function decreases during the period, which can be attributed to the inverse storage effect in young water. The linearly-scaled SAS function simulated increasing concentration during the period because the tracer-labeled water gets old and moves to the older age-ranked storage where it is more preferentially discharged. The observed concentration remains more or less the same during the period, meaning that there was an insignificant change in the preference when the tracer-labeled water moves to the older age-ranked storage.

The QSS approach performed better for the case of miniLEO. The QSS SAS function for $P \to \infty$ closely captures the upper and the lower envelope of the observed SAS functions, although details in the observed SAS function are not captured (Figures 10b–1). The QSS SAS function for $P = 1.0$ m better reproduces the covex part of the SAS function during wet conditions (Figures 10b–2). It also reproduces the convex part of the SAS function during dry conditions but not the concave part over the younger age-ranked storage. The observed inverse storage effect is reproduced in both cases. Both SAS functions reproduce the observed BTCs reasonably well (Figure 10a). As the convexity increases the discharge of younger water, the SAS function with $P = 1.0$ m estimates higher concentration during the early time and better reproduces several peaks of the observed BTC.

This application shows that the hydraulic theory-based SAS function framework developed here can provide good predictions of hillslope transport under these experimental conditions. It has also revealed several important limitations.

First, methods to impart time-variability to the estimated SAS function need to be further developed and tested in more hydrologic systems. The quasi-steady state approach shows promise in the application to miniLEO. A preliminary result in Kim (2018) suggests the quasi-steady state approach has the potential to reproduce time-variable transport dynamics in a real-world catchment with a sharp exponential decline in the saturated hydraulic conductivity with depth. However, in the LEO west hillslope, the QSS approach does not reproduce the observed time-variability. For the cases considered, estimating the temporal variation of the water table profile and the unsaturated zone storage is an important factor in reproducing the time-variability of the observed SAS function. In miniLEO, we used the observed unsaturated zone storage and the saturated zone storage, and the hydraulic

theory provides a good approximation of the observed water table around the downslope boundary. The kinematic wave model applied for the LEO west hillslope estimates the downslope water table based on soil hydraulic and geomorphologic properties and the flux at each time. The model may underestimate the water table and overestimated the unsaturated zone storage at the dry condition, resulting in the large shift of the hillslope scale SAS function that leads to the inverse storage effect. This situation can potentially be improved by utilizing the hillslope-storage Boussinesq equation (Troch et al., 2003) and by imposing the downslope water table boundary condition using observed water table data around the downslope boundary. However, the consequence of assuming the quasi-steady state requires further investigation.

Second, the effect of unaccounted processes and flow pathways in the model of the SAS function needs to be better understood. This is important both in predicting the SAS function as well as in understanding the hydrologic transport of a system when an observed SAS function exists. For example, a numerical study by Kim (2018) showed that the relative contribution of lateral flow in the unsaturated zone to the discharge is larger under drier conditions in the LEO west hillslope. Such a piece of knowledge can help understanding the difference between the hydraulic-theory based SAS function and the observed SAS function; The observed SAS function shows younger water transport compared to the hydraulic-theory-based SAS function under relatively dry conditions. This may be due to ongoing drainage from the unsaturated zone that is not accounted for. The concavity of the observed miniLEO SAS function over the young storage might also be due to the unaccounted processes such as dispersion. The theoretical framework may produce tighter predictions if such processes were included.

Despite those limitations, the hydraulic theory-based SAS function improves our ability to predict BTC (without calibration) and to explain the form of the SAS function. Where no other information about the shape of the SAS function exists, a reasonable first guess for the SAS function might be the uniform distribution (Harman, 2015), which represents the transport mechanism referred to as ”uniform sampling” (or ”random sampling”). The hydraulic theory-based SAS function improves on this by utilizing the hydraulic properties of the hydrologic system, leading to significant improvement in the BTC prediction compared to the use of the uniform SAS function (see Figures 9a-2 and Figures 10a-2). Furthermore, the framework provides a way to explain the form of the SAS function. It helps to characterize the transport dynamics in the LEO west hillslope based on Hi and the convergent topography. For miniLEO, the convexity of the SAS function might be due to the vertical structure of the soil hydraulic conductivity. It also allows us to hypothesize missing components in the model by comparing the observed and the modeled BTCs or the observed and the estimated SAS functions.

5. Conclusions

In this study, we developed a simple process-based model to predict the transit time distributions, the StorAge Selection (SAS) functions, and the internal hydro-chronological structures at the hillslope scale with steady infiltration. The developed theoretical framework first considers unsaturated zone and saturated zone flow and transport separately and combines those to estimate the hillslope scale transport closures. The framework is based upon several simplifications of flow and transport processes using the well-known assumptions such as: Dupuit-Forchheimer assumption for saturated zone flow and transport, and vertical flow and transport dominance in the unsaturated zone.

The current framework was developed and applied for the idealized virtual hillslopes with exponential saturated hydraulic conductivity declines along the depth. Analytical solutions for predicting water table, unsaturated zone flow, and transport, and saturated zone flow and transport are derived, in some cases, with additional assumptions such as the assumption of effective thickness (semi-confined) aquifer for the saturated zone transport. The developed theoretical framework was validated by comparing the estimated water table and the SAS functions to those estimated using the higher-order numerical model—ParFlow and SLIM-FAST. We also illustrated the usefulness of the framework by applying it to the two experimental systems with contrasting Hillslope numbers. The framework estimated the steady state SAS function close to the observed SAS functions and help us explain the difference in the SAS function observed in the systems.

The simplified framework furthermore allowed us to define several dimensionless numbers, characterizing flow and transport. The hybrid model for estimating water table shows that the effect of water table gradient is

negligible when $Hi_X > 10$, and, in that case, the model is similar to the original version of TOPMODEL. The SAS function for saturated zone converges to the exponential function when $P^* > 5$ and to the linear function when $P^* \to 0$. The convergence to the exponential function implies that the effect of large-scale variations in bedrock topography on transport is limited when $P^* > 5$, and total water storage is not important when the condition holds. The two regimes for the internal age structure were also identified: the 'scaled lateral symmetry' for $P^* \to 0$ and the 'water table parallel' for $P^* > 5$. While we looked at the age structure to understand the links between the internal structures and the SAS functions, those identified regimes would be useful to further develop simple process-based bedrock weathering models like those discussed in Harman and Kim (2019).

The framework, however, was developed for simple and idealized systems, and it built upon many assumptions and simplifications. The framework was developed under steady state assumption, the assumption of negligible local dispersion, negligible spatial (random) heterogeneity in hydraulic conductivity, Darcy-Richards paradigm, and so on. Adding more processes and relaxing the assumptions will be tasks for future study, and we hope the developed framework would serve as a basis to add such complexities. For example, one apparent and direct path toward such generalization would be adding the transport dynamics into the hillslope-storage Boussinesq model (Troch et al., 2003), which would allow one to consider diverse shapes of hillslopes. For example, Kim, Volkmann, et al. (2022) consider the diverse plan shape of hillslope using the hillslope-storage kinematic wave model of Troch et al. (2002).

Even with the limitations and the simplifications, we expect that this basic framework could be useful in several ways. First, we may use it to obtain a first-order guess for the forms of TTD and SAS at the hillslope scale. The first order guess can then be compared to the estimated SAS functions based on the tracer dataset to frame the hypothesis on internal transport dynamics. Note that other processes could lead to similar forms of the SAS functions, and so correspondence with observed tracer data supports but does not confirm the estimate. Nevertheless, as the hypothesis is based on the soil hydraulic properties and the geomorphologic structure of a system, other data can be collected to further validate (or invalidate) the theory and its assumptions. For example, for the cases considered in this study, the spatial pattern of water table depth, hydraulic conductivity profile (that is either measured or inferred using flow data), or depth-dependent water age would be useful to validate the first order hypothesis by comparing those to the spatial pattern of the estimated water table depth (e.g., see Figure 5) and the internal age structure (e.g., see Figure 3 or Figure 7). In addition, the first order guess could serve as a functional form of the SAS function in the usual calibration procedure. The physically meaningful parameters in the form can then be calibrated using tracer datasets when those values are not available, and such application would yield first order guess on those values. This application is possible since the steady state SAS functions can be used directly in unsteady-state modeling, unlike steady state TTDs which fail to keep the mass balance.

Second, the analytical solutions can be generalized to unsteady state solutions directly using the quasi-steady state assumption (e.g., Verhoest & Troch, 2000; Akylas et al., 2015), which further allows us to do the previously described applications considering the internal flow pathway variability. However, as we discussed in Section 4, its applicability and methods of application (e.g., imposing an observed water table data as a boundary condition to better simulate the unsaturated zone storage that does not contribute to discharge) need to be further investigated. Furthermore, the presented analytical solutions for the TTDs are a generalization of the widely applied ground water transport model of Vogel (1966) and Małoszewski and Zuber (1982), that has been applied widely for tracer-based water age estimation, such as tritium dating (e.g., Ma et al., 2019), and those TTDs (or the SAS functions) can be applied to model the transport considering the exponential decline. We furthermore expect the derived dimensionless numbers to be useful in classifying the hillslope scale water flow and transport dynamics.

Appendix A: Generalized TOPMODEL Prediction of the Water Table Depth

Originally, TOPMODEL estimates the depth to the water table D based on the assumption that the hydraulic gradient can be assumed to be parallel to the soil surface slope (Beven & Kirkby, 1979). This assumption can be easily relaxed by replacing $\tan\beta$ by the water table gradient $\frac{d(H(x)-D(x))}{dx}$ as:

$$\frac{d(H(x)-D(x))}{dx} k_0 \int_0^{H(x)-D(x)} e^{-(H(x)-z)/P} dz = Jx \tag{A1}$$

or in its derivative form as:

$$\frac{dY(x)}{dx}\frac{dh(x)}{dx} + Y(x)\frac{d^2h(x)}{dx^2} + \frac{J}{k_0 P} = 0 \tag{A2}$$

where $Y(x) = e^{-H(x)/P}(e^{h(x)/P} - 1)$.

As an analogy to the analysis done for Boussinesq aquifer with sloping bedrock, we may define a type of Hillslope (peclet) number and use it as a measure of how the model is close to the original TOPMODEL since TOPMODEL works when advection (of water energy) dominates.

To do so, we may linearize the differentiated governing equation. The governing Equation A2 can be linearized if we remove $h(x)$ dependency of $Y(x)$. Let us do this by assuming $h(x)$ in $Y(x)$ as H_l which gives: $Y(x) = e^{-H(x)/P}\left(e^{H_l/P} - 1\right)$. Then the exponential Hillslope number Hi_X can be written as:

$$\mathrm{Hi}_X = \frac{L}{2Y(x)}\frac{dY(x)}{dx} = \frac{L\tan\beta}{2P} \tag{A3}$$

The exponential Hillslope number Hi_X has a very similar functional form to the Hillslope number Hi which is $\frac{L\tan\eta}{2\bar{H}}$, where $\bar{H}$ is the effective water table height and η is the slope of the impermeable layer. In Hi_X, P is the depth where the hydraulic conductivity is 0.37 ($= e^{-1}$) of its surface value (or where 63% of transmissivity at saturation is above the depth) and replacing the effective depth $\bar{H}$ in the original Hillslope number Hi.

The model (A1) is a non-linear first order differential equation that can be solved with a boundary condition at the most downslope at $x = L$. The upslope boundary condition is $dh/dx = 0$, since $q = 0$ at $x = 0$. In terms of the downslope boundary condition, we considered two cases: the Neumann boundary condition and Dirichlet condition.

The solution for the Dirichlet boundary condition is presented in Equation (11). For a Neumann boundary condition $\frac{dD(x)}{dx} = \epsilon$, the solution for D is the same, but with $\hat{R}_L$ defined as:

$$\hat{R}_L = \frac{\ln\left(1 + \frac{2\mathrm{Hi}_X}{1+\epsilon} M e^{2\mathrm{Hi}_X \hat{H}_L}\right) - 1}{2\mathrm{Hi}_X} + M e^{2\mathrm{Hi}_X \hat{H}_L}\left(\frac{1}{2\mathrm{Hi}_X} + 1 - \frac{1}{1+\epsilon}\right) \tag{A4}$$

Using the same symbols, the TOPMODEL depth to water table can be re-written as: $\hat{D}(\hat{x}) = \hat{P}\ln\left(1/\left(e^{-\hat{H}(\hat{x})/\hat{P}} + M\hat{x}/\hat{P}\right)\right)$, and the associated water table gradient $\hat{h}(\hat{x})$ $(= \hat{H}(\hat{x}) - \hat{D}(\hat{x}))$ is:

$$\frac{d\hat{h}}{d\hat{x}} = \frac{1 + M e^{2\mathrm{Hi}_X \hat{H}(\hat{x})}}{1 + 2\mathrm{Hi}_X M e^{2\mathrm{Hi}_X \hat{H}(\hat{x})}\hat{x}} - 1 \tag{A5}$$

In TOPMODEL, the estimated water table gradient is actually different from head gradient driving flow (i.e., the topographic gradient), especially when $\hat{x}$ is small. (Note that in the dimensionless units the gradient of surface is -1). We examined the difference between TOPMODEL and the hybrid model by plotting the predicted values of $\hat{h}(\hat{x})$ for the case of $\epsilon = 0$ which sets the downslope boundary condition identical to the hydraulic gradient in TOPMODEL. The water table profiles are functions of M, Hi_X and H_L. We examined the effect of Hi_X at different $M \in \{0.01, 0.05, 0.1\}$. $\hat{H}_L$ has only a weak control, determining only the elevation of the topography above the water table and not the form of the water table itself, so $\hat{H}_L$ was chosen in each case such that $\hat{H}_L = 2\hat{h}(1)$—that is, the water table intersects the downslope boundary halfway up the subsurface domain). Figure A1 shows the results. Overall, Equation (11) is close to that of TOPMODEL as Hi_X increases. However, the new model does not converge to the original TOPMODEL, especially at the upslope, since TOPMODEL requires $D \to \infty$ at $x = 0$.

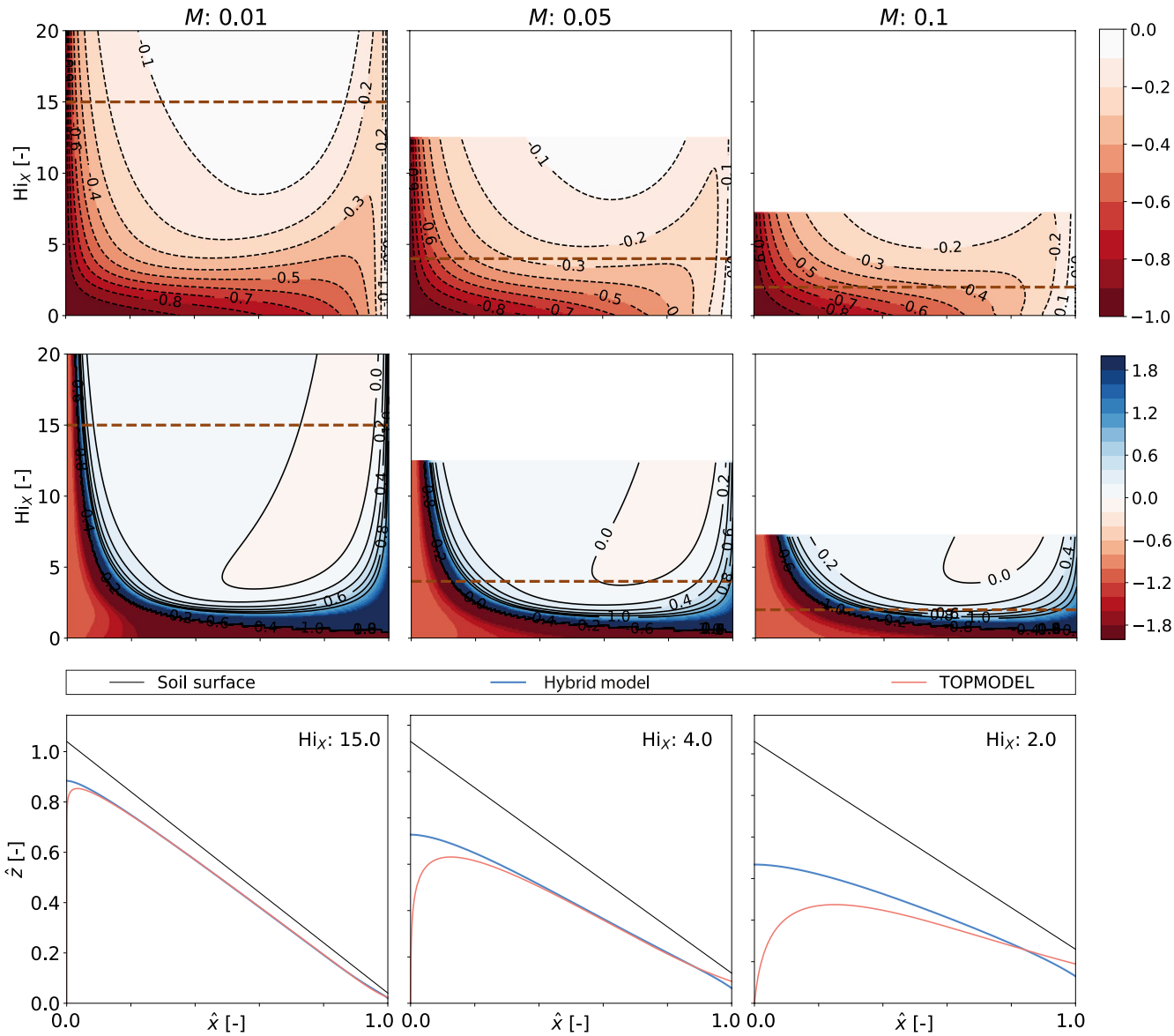

Figure A1. Differences between the hybrid model and TOPMODEL for the fixed gradient boundary condition. (top) The difference in the hydraulic head, (middle) the difference in water table gradient, (bottom) some examples of water table prediction.

Notation

t	Time
$\boldsymbol{x}$	$\boldsymbol{x} = (x, y, z)$ is Cartesian spatial coordinate/or Lagrangian coordinate of a particle n when it used as $\boldsymbol{x}(\cdot, n)$
z'	Depth from the soil surface; $z' = H - z$
$x_0(T_s)$	The x-directional injection location of a water particle that has the saturated zone transit time T_s.
z_d	$z_d(x', x_0)$ is the vertical location of a particle at x' which can be determined by its injection location x_0.
D	Depth to water table
θ	Water content
θ_s	Saturated water content
θ_r	Residual water content
k	Hydraulic conductivity

k_s	Saturated hydraulic conductivity
k_0	Saturated hydraulic conductivity at the soil surface ($z = H$ or $D = 0$)
k_r	Relative hydraulic conductivity as a function of ψ.
ψ	suction head that is negative when soil is unsaturated
ψ_A	Van Genuchten soil water retention curve parameter
n	Van Genuchten soil water retention curve parameter
m	Van Genuchten soil water retention curve parameter; $m = 1 - 1/n$.
$\boldsymbol{V}$	Velocity vector
V_x	The x-directional component of water particle velocity
H	Soil surface profile of hillslopes
H_e	Thickness of the effective thickness (or semi-confined) aquifer
H_L	Soil thickness at the downslope boundary ($x = L$)
L	Hillslope length
$\tan\beta$	Topographic slope
P	The length scale of the exponential decline of saturated hydraulic conductivity with depth
h	Hydraulic head
h_L	Hydraulic head at the downslope boundary
S_T	Age-ranked storage
Ω_Q	StorAge Selection function
$\Omega_{Q,u}$	StorAge Selection function for unsaturated zone
$\overleftarrow{P_Q}$	Time-variable backward (cumulative) transit time distribution
J	Infiltration rate or recharge rate; those are the same under steady state
Q	Outflux rate and $Q = J$ in this study because of the steady state assumption
P_Q	Cumulative transit time distribution
$P_{Q,s}$	Cumulative transit time distribution for saturated zone
$P_{Q,u}$	Cumulative transit time distribution for unsaturated zone
$P_{Q,u,s}(T_u, T_s)$	The joint distribution of T_u and T_s.
p_Q	Transit time distribution
A	Age
LE	Life expectancy
T	Transit time
T_u	Transit time in the unsaturated zone
T_s	Transit time in the saturated zone
S_u	Unsaturated zone storage
ϕ	Drainable porosity
Hi_X	Exponential Hillslope number
Hi_u	Unsaturated zone Hillslope number with the exponential saturated hydraulic conductivity decline with depth
Da_u	Unsaturated zone dimensionless number
P^*	Saturated zone transport number
K_H	Transmissivity

Acknowledgments
The authors gratefully acknowledge the support of the National Science Foundation grant EAR-1344552, EAR-1417175, EAR-1654194, EAR-2120113, and GCR-2121155. We appreciate the reviewers and the editors for their constructive advice. We thank our colleagues who co-conducted the experiments presented in Section 4: Luke A. Pangle, Till H. M. Volkmann, Yadi Wang, Antonio A. Meira Neto, Katerina Matos, Marco Lora, Charlene Cardoso, Nate Abramson, Aaron Bugaj, Michael Sibayan, Edward A. Hunt, and Peter Troch.

Data Availability Statement

The LEO West hillslope data and the miniLEO data are available in Hydroshare; See Kim, Volkmann, Wang, et al. (2021) and Kim, Pangle, et al. (2022).

References

Abramowitz, M., & Stegun, I. A. (1974). *Handbook of mathematical functions, with Formulas, Graphs, and mathematical tables*. Dover Publications.

Akylas, E., Gravanis, E., & Koussis, A. D. (2015). Quasi-steady flow in sloping aquifers Evangelos. *Water Resources Research*, *51*, 9165–9181. https://doi.org/10.1002/2014WR016651

Ameli, A., McDonnell, J., & Bishop, K. (2016). The exponential decline in saturated hydraulic conductivity with depth: A novel method for exploring its effect on water flow paths and transit time distribution. *Hydrological Processes*, *30*, 2438–2450. https://doi.org/10.1002/hyp.10777

Benettin, P., Rinaldo, A., & Botter, G. (2013). Kinematics of age mixing in advection-dispersion models. *Water Resources Research*, *49*(12), 8539–8551. https://doi.org/10.1002/2013WR014708

Benettin, P., Soulsby, C., Birkel, C., Tetzlaff, D., Botter, G., & Rinaldo, A. (2017). Using SAS functions and high-resolution isotope data to unravel travel time distributions in headwater catchments. *Water Resource Research*, *53*, 5375–5377. https://doi.org/10.1002/2013WR014979.Repl

Berne, A., Uijlenhoet, R., & Troch, P. A. (2005). Similarity analysis of subsurface flow response of hillslopes with complex geometry. *Water Resources Research*, *41*, 1–10. https://doi.org/10.1029/2004WR003629

Beven, K. (1982). On subsurface stormflow: An analysis of response times. *Hydrological Sciences Journal*, *27*(4), 505–521. https://doi.org/10.1080/02626668209491129

Beven, K. J., & Kirkby, M. J. (1979). A physically based, variable contributing area model of basin hydrology. *Hydrological Sciences Bulletin*, *24*(1), 43–69. https://doi.org/10.1080/02626667909491834

Boussinesq, J. (1877). *Essai sur la théorie des eaux courantes*. Imprimerie Nationale.

Bredenkamp, D., & Vogel, J. (1970). Study of a dolomitic aquifer with carbon-14 and tritium. In *Isotope hydrology 1970 Proceedings of a symposium* (pp. 349–372). International Atomic Energy Agency (IAEA).

Brutsaert, W. (1994). The unit response of groundwater outflow from a hillslope. *Water Resources Research*, *30*(10), 2759–2763. https://doi.org/10.1029/94WR01396

Bryson, M. C. (1974). Heavy-tailed distributions: Properties and tests. *Technometrics*, *16*(1), 61–68.

Cook, P. G., & Böhlke, J.-K. (2000). Determining Timescales for groundwater flow and Solute transport. In P. G. Cook, & A. L. Herczeg (Eds.), *Environmental tracers in subsurface hydrology*. (pp. 1–30). Springer US.

Corless, R. M., Gonnet, G. H., Hare, D. E. G., Jeffrey, D. J., & Knuth, D. E. (1996). On the Lambert W function. *Advances in Computational Mathematics*, *5*(1), 329–359. https://doi.org/10.1007/BF02124750

Cornaton, F., & Perrochet, P. (2006). Groundwater age, life expectancy and transit time distributions in advective–dispersive systems: 1. Generalized reservoir theory. *Advances in Water Resources*, *29*(9), 1267–1291. https://doi.org/10.1016/j.advwatres.2005.10.009

Cox, D. R., & Miller, H. D. (1972). *The Theory of stochastic processes*. : Chapman and Hall, cop. 1965.

Etcheverry, D. (2001). *Une approche déterministe des distributions des temps de transit de l'eau souterraine par la théorie des réservoirs*. : Ph.D. thesis, University of Neuchâtel.

Fiori, A., Russo, D., & Di Lazzaro, M. (2009). Stochastic analysis of transport in hillslopes: Travel time distribution and source zone dispersion. *Water Resources Research*, *45*(8), 1–13. https://doi.org/10.1029/2008WR007668

Gelhar, L. W., & Wilson, J. L. (1974). Ground-water quality modeling. *Ground Water*, *12*(6), 399–408. https://doi.org/10.1111/j.1745-6584.1974.tb03050.x

Godsey, S. E., Aas, W., Clair, T. A., de Wit, H. A., Fernandez, I. J., Kahl, J. S., et al. (2010). Generality of fractal 1/f scaling in catchment tracer time series, and its implications for catchment travel time distributions. *Hydrological Processes*, *24*(12), 1660–1671. https://doi.org/10.1002/hyp.7677

Gomez, J. D., & Wilson, J. L. (2013). Age distributions and dynamically changing hydrologic systems: Exploring topography-driven flow. *Water Resources Research*, *49*(3), 1503–1522. https://doi.org/10.1002/wrcr.20127

Haitjema, H. (1995). On the residence time distribution in idealized groundwatersheds. *Journal of Hydrology*, *172*(1–4), 127–146. https://doi.org/10.1016/0022-1694(95)02732-5

Harman, C. J. (2015). Time-variable transit time distributions and transport: Theory and application to storage-dependent transport of chloride in a watershed. *Water Resources Research*, *51*, 1–30. https://doi.org/10.1002/2014WR015707

Harman, C. J., & Kim, M. (2014). An efficient tracer test for time-variable transit time distributions in periodic hydrodynamic systems. *Geophysical Research Letters*, *41*, 1567–1575. https://doi.org/10.1002/2013GL058980

Harman, C. J., & Kim, M. (2019). A low-dimensional model of bedrock weathering and lateral flow coevolution in hillslopes: 1. Hydraulic theory of reactive transport. *Hydrological Processes*, *33*(4), 466–475. https://doi.org/10.1002/hyp.13360

Harman, C. J., & Sivapalan, M. (2009). A similarity framework to assess controls on shallow subsurface flow dynamics in hillslopes. *Water Resources Research*, *45*(1), 1–12. https://doi.org/10.1029/2008WR007067

Hogg, R. V., McKean, J. W., & Craig, A. T. (2005). *Introduction to mathematical statistics*. Pearson Education.

Johnson, N. L., Kotz, S., & Balakrishnan, N. (1994). *Continuous Univariate Distributions* (2nd ed., Vol. 1). Wiley.

Johnson, N. L., Kotz, S., & Balakrishnan, N. (1995). *Continuous Univariate Distributions* (2nd ed., Vol. 2). Wiley.

Jones, J. E., & Woodward, C. S. (2001). Newton–Krylov-multigrid solvers for large-scale, highly heterogeneous, variably saturated flow problems. *Advances in Water Resources*, *24*(7), 763–774. https://doi.org/10.1016/S0309-1708(00)00075-0

Kim, M. (2018). *Processes and landscape structure underlying system scale hydrologic transport: Theory, experiment, and modeling, Doctoral Dissertation*. Johns Hopkins University.

Kim, M., Pangle, L., Cardoso, C., Volkmann, T. H. M., Wang, Y., Harman, C. J., et al. (2022). Biosphere 2 Landscape Evolution Observatory miniLEO PERTH Experiment Dataset, *HydroShare* [Data set]. https://doi.org/10.4211/hs.2a07b89d97334654859c62f178cdeb0d

Kim, M., Pangle, L. A., Cardoso, C., Lora, M., Volkmann, T. H. M., Wang, Y., et al. (2016). Transit time distributions and StorAge Selection functions in a sloping soil lysimeter with time-varying flow paths: Direct observation of internal and external transport variability. *Water Resources Research*, *52*(9), 7105–7129. https://doi.org/10.1002/2016WR018620

Kim, M., & Troch, P. A. (2020). Transit Time Distributions Estimation Exploiting Flow-Weighted Time: Theory and Proof-of-Concept. *Water Resources Research*, *56*(12). https://doi.org/10.1029/2020wr027186

Kim, M., Volkmann, T. H. M., Bugaj, A., Wang, Y., Meira Neto, A. A., Matos, K., et al. (2021). Uncovering the hillslope scale flow and transport dynamics in an experimental hydrologic system. *Hydrological Processes*, *35*(8). https://doi.org/10.1002/hyp.14337

Kim, M., Volkmann, T. H. M., Wang, Y., Meira Neto, A. A., Matos, K., Harman, C. J., & Troch, P. A. (2021). Biosphere 2 landscape evolution observatory 2016 PERTH experiment - dataset for the LEO east and west hillslopes. *HydroShare*. https://doi.org/10.4211/hs.a74168d3396c436a8f0cd5910358df13

Kim, M., Volkmann, T. H. M., Wang, Y., Meira Neto, A. A., Matos, K., Harman, C. J., & Troch, P. A. (2022). Direct Observation of Hillslope Scale StorAge Selection Functions in Experimental Hydrologic Systems: Geomorphologic Structure and Preferential Discharge of Old Water. *Water Resources Research*, *58*(3). https://doi.org/10.1029/2020wr028959

Kirchner, J., Feng, X., & Neal, C. (2000). Fractal stream chemistry and its implications for contaminant transport in catchments. *Nature*, *403*(6769), 524–527. https://doi.org/10.1038/35000537

Kirchner, J. W. (2019). Quantifying new water fractions and transit time distributions using ensemble hydrograph separation: theory and benchmark tests. *Hydrology and Earth System Sciences*, *23*(1), 303–349. https://doi.org/10.5194/hess-23-303-2019

Kirchner, J. W., Feng, X., & Neal, C. (2001). Catchment-scale advection and dispersion as a mechanism for fractal scaling in stream tracer concentrations. *Journal of Hydrology*, *254*(1–4), 82–101. https://doi.org/10.1016/S0022-1694(01)00487-5

Kollet, S. J., & Maxwell, R. M. (2006). Integrated surface–groundwater flow modeling: A free-surface overland flow boundary condition in a parallel groundwater flow model. *Advances in Water Resources*, *29*(7), 945–958. https://doi.org/10.1016/j.advwatres.2005.08.006

Koussis, A. (1992). A linear conceptual subsurface storm flow model. *Water Resources Research*, *28*(4), 1047–1052.

Leray, S., de Dreuzy, J. R., Bour, O., Labasque, T., & Aquilina, L. (2012). Contribution of age data to the characterization of complex aquifers. *Journal of Hydrology*, *464–465*, 54–68. https://doi.org/10.1016/j.jhydrol.2012.06.052

Leray, S., Engdahl, N. B., Massoudieh, A., Bresciani, E., & McCallum, J. (2016). Residence time distributions for hydrologic systems: Mechanistic foundations and steady state analytical solutions. *Journal of Hydrology*, *543*, 67–87. https://doi.org/10.1016/j.jhydrol.2016.01.068

Luther, K. H., & Haitjema, H. M. (1998). Numerical experiments on the residence time distributions of heterogeneous groundwatersheds. *Journal of Hydrology*, *207*(1–2), 1–17. https://doi.org/10.1016/S0022-1694(98)00112-7

Ma, B., Jin, M., Liang, X., & Li, J. (2019). Application of environmental tracers for investigation of groundwater mean residence time and aquifer recharge in fault-influenced hydraulic drop alluvium aquifers. *Hydrology and Earth System Sciences*, *23*(1), 427–446. https://doi.org/10.5194/hess-23-427-2019

Maher, K. (2011). The role of fluid residence time and topographic scales in determining chemical fluxes from landscapes. *Earth and Planetary Science Letters*, *312*, 48–58. https://doi.org/10.1016/j.epsl.2011.09.040

Małoszewski, P., & Zuber, a. (1982). Determining the turnover time of groundwater systems with the aid of environmental tracers: 1. Models and their applicability. *Journal of Hydrology*, *57*(3–4), 207–231. https://doi.org/10.1016/0022-1694(82)90147-0

Maxwell, R. M., Kollet, S. J., Smith, S. G., Woodward, C. S., Falgout, R. D., Ferguson, I. M., et al. (2014). *ParFlow User's Manual, International ground water modeling center Report GWMI*.

Maxwell, R. M., & Thomson, A. F. B. (2006). *SLIM-FAST : A User's Manual*. The Regents of the University of California.

McGuire, K. J., & McDonnell, J. J. (2006). A review and evaluation of catchment transit time modeling. *Journal of Hydrology*, *330*(3–4), 543–563. https://doi.org/10.1016/j.jhydrol.2006.04.020

Morgenstern, U., Stewart, M. K., & Stenger, R. (2010). Dating of streamwater using tritium in a post nuclear bomb pulse world: Continuous variation of mean transit time with streamflow. *Hydrology and Earth System Sciences*, *14*(11), 2289–2301. https://doi.org/10.5194/hess-14-2289-2010

Pangle, L. A., DeLong, S. B., Abramson, N., Adams, J., Barron-Gafford, G. A., Breshears, D. D., et al. (2015). The landscape Evolution observatory: A large-scale controllable infrastructure to study coupled Earth-surface processes. *Geomorphology*, *244*, 190–203. https://doi.org/10.1016/j.geomorph.2015.01.020

Pangle, L. A., Kim, M., Cardoso, C., Lora, M., Volkmann, T. H. M., Wang, Y., et al. (2017). The mechanistic basis for storage-dependent age distributions of water discharged from an experimental hillslope. *Water Resources Research*, *53*(4), 2733–2754. https://doi.org/10.1002/2016WR019901

Pickands, J. (1975). Statistical inference using extreme order statistics. *Annals of Statistics*, *3*(1), 119–131.

Pollock, D. W. (1988). Semianalytical computation of path lines for finite-difference models. *Groundwater*, *26*(6), 743–750. https://doi.org/10.1111/j.1745-6584.1988.tb00425.x

Raats, P. (1978). Convective transport of solutes by steady flows II. Specific flow problems. *Agricultural Water Management*, *1*, 219–232.

Rinaldo, A., Benettin, P., Harman, C. J., Hrachowitz, M., Mcguire, K. J., Velde, Y. V. D., et al. (2015). Storage selection functions: A coherent framework for quantifying how catchments store and release water and solutes. *Water Resources Research*, *51*, 1–8. https://doi.org/10.1002/2015WR017273

Rodriguez, N. B., Benettin, P., & Klaus, J. (2020). Multimodal water age distributions and the challenge of complex hydrological landscapes. *Hydrological Processes*, *34*, 2707–2724. https://doi.org/10.1002/hyp.13770

Rupp, D. E., & Selker, J. S. (2005). Drainage of a horizontal Boussinesq aquifer with a power law hydraulic conductivity profile. *Water Resources Research*, *41*(11), 1–8. https://doi.org/10.1029/2005WR004241

Sidle, R. C., Noguchi, S., Tsuboyama, Y., & Laursen, K. (2001). A conceptual model of preferential flow systems in forested hillslopes: Evidence of self-organization. *Hydrological Processes*, *15*(10), 1675–1692. https://doi.org/10.1002/hyp.233

Taylor, G. (1953). Dispersion of soluble matter in solvent flowing slowly through a tube. *Proceedings of the Royal Society A: Mathematical, Physical & Engineering Sciences*, *219*, 186–203. https://doi.org/10.1098/rspa.1953.0139

Troch, P. A., Berne, A., Bogaart, P., Harman, C., Hilberts, A. G. J., Lyon, S. W., et al. (2013). The importance of hydraulic groundwater theory in catchment hydrology: The legacy of Wilfried Brutsaert and Jean-Yves Parlange. *Water Resources Research*, *49*(9), 5099–5116. https://doi.org/10.1002/wrcr.20407

Troch, P. A., Paniconi, C., & Emiel van Loon, E. (2003). Hillslope-storage Boussinesq model for subsurface flow and variable source areas along complex hillslopes: 1. Formulation and characteristic response. *Water Resources Research*, *39*(11), 1316. https://doi.org/10.1029/2002WR001728

Troch, P. A., van Loon, E., & Hilberts, A. G. J. (2002). Analytical solutions to a hillslope-storage kinematic wave equation for subsurface flow. *Advances in Water Resources*, *25*, 637–649. https://doi.org/10.1016/S0309-1708(02)00017-9

van den Heuvel, D. B., Troch, P. A., Booij, M. J., Niu, G. Y., Volkmann, T. H. M., & Pangle, L. A. (2018). Effects of differential hillslope-scale water retention characteristics on rainfall-runoff response at the Landscape Evolution Observatory. *Hydrological Processes*, *32*, 2118–2127. https://doi.org/10.1002/hyp.13148

van der Velde, Y., Heidbüchel, I., Lyon, S. W., Nyberg, L., Rodhe, A., Bishop, K., & Troch, P. a. (2014). Consequences of mixing assumptions for time-variable travel time distributions. *Hydrological Processes*, *29*(16), 3460–3474. https://doi.org/10.1002/hyp.10372

van der Velde, Y., Torfs, P. J. J. F., van der Zee, S. E. A. T. M., & Uijlenhoet, R. (2012). Quantifying catchment-scale mixing and its effect on time-varying travel time distributions. *Water Resources Research*, *48*(6), W06–W536. https://doi.org/10.1029/2011WR011310

van Genuchten, M. T. (1980). A closed-form equation for predicting the hydraulic conductivity of unsaturated soils. *Soil Science Society of America Journal*, *44*(5), 892. https://doi.org/10.2136/sssaj1980.03615995004400050002x

van Meerveld, H. J. I., Kirchner, J. W., Vis, M. J. P., Assendelft, R. S., & Seibert, J. (2019). Expansion and contraction of the flowing stream network alter hillslope flowpath lengths and the shape of the travel time distribution. *Hydrology and Earth System Sciences*, *23*, 4825–4834. https://doi.org/10.5194/hess-23-4825-2019

Verhoest, N. E., & Troch, P. A. (2000). Some analytical solutions of the linearized Boussinesq equation with recharge for a sloping aquifer. *Water Resources Research*, *36*(3), 793–800. https://doi.org/10.1029/1999WR900317

Vogel, J. (1966). *Investigation of groundwater flow with radiocarbon, Isotope hydrology 1966 Proceedings of a symposium*.

Wackerly, D. D., III, W. M., & Scheaffer, R. L. (2002). *Mathematical statistics with applications* (6th ed.,). Elsevier.

Wilusz, D. C., Harman, C. J., & Ball, W. P. (2017). Sensitivity of catchment transit times to rainfall variability under present and future climates. *Water Resources Research*, *53*(12), 10231–10256. https://doi.org/10.1002/2017WR020894

Zuber, A., Witczak, S., Różański, K., Śliwka, I., Opoka, M., Mochalski, P., et al. (2005). Groundwater dating with3H and SF6 in relation to mixing patterns, transport modelling and hydrochemistry. *Hydrological Processes*, *19*(11), 2247–2275. https://doi.org/10.1002/hyp.5669